Chemical Geology 426 (2016) 118–134

Contents lists available at ScienceDirect

Chemical Geology

journal homepage: www.elsevier.com/locate/chemgeo

Trace-element geochemistry and U–Pb dating of perovskite in kimberlites of the Lunda Norte province (NE Angola): Petrogenetic and tectonic implications

Montgarri Castillo-Oliver [a,b,*], Salvador Galí [a], Joan Carles Melgarejo [a], William L. Griffin [b], Elena Belousova [b], Norman J. Pearson [b], Manuel Watangua [c], Suzanne Y. O'Reilly [b]

[a] Department de Cristal·lografia, Mineralogia i Dipòsits Minerals, Universitat de Barcelona, Martí i Franquès s/n, 08028 Barcelona, Catalonia, Spain
[b] ARC Centre of Excellence for Core to Crust Fluid Systems and GEMOC, Department of Earth and Planetary Sciences, Macquarie University, NSW 2019, Australia
[c] Sociedade Mineira de Catoca, Catoca, Lunda Sul, Angola

ARTICLE INFO

Article history:
Received 22 May 2015
Received in revised form 24 September 2015
Accepted 23 December 2015
Available online 14 January 2016

Keywords:
U–Pb geochronology
Angolan kimberlites
Lunda Norte
Perovskite
Mineral chemistry
Magma mingling

ABSTRACT

Perovskite ($CaTiO_3$) has become a very useful mineral for dating kimberlite eruptions, as well as for constraining the compositional evolution of a kimberlitic magma and its source. Despite the undeniable potential of such an approach, no similar study had been done in Angola, the fourth largest diamond producer in Africa. Here we present the first work of in situ U–Pb geochronology and Sr–Nd isotope analyses of perovskite in six Angolan kimberlites, supported by a detailed petrographic and geochemical study of their perovskite populations. Four types of perovskite were identified, differing in texture, major- and trace-element composition, zoning patterns, type of alteration and the presence or absence of inclusions. Primary groundmass perovskite is classified either as anhedral, Na-, Nb- and LREE-poor perovskite (Ia); or euhedral, strongly zoned, Na-, Nb- and LREE-rich perovskite (Ib). Secondary perovskite occurs as reaction rims on ilmenite (IIa) or as high Nb (up to 10.6 wt% Nb_2O_5) perovskite rims on primary perovskite (IIb). The occurrence of these four types within the Mulepe kimberlites is interpreted as an evidence of a complex, multi-stage process that involved mingling of compositionally different melts.

U–Pb dating of these perovskites yielded Lower Cretaceous ages for four of the studied kimberlites: Mulepe 1 (116.2 ± 6.5 Ma), Mulepe 2 (123.0 ± 3.6 Ma), Calonda (119.5 ± 4.3 Ma) and Cat115 (133 ± 10 Ma). Kimberlite magmatism occurred in NE Angola likely due to reactivation of deep-seated translithospheric faults (>300 km) during the break-up of Gondwana. Sr–Nd isotope analyses of four of these kimberlites indicate that they are Group I kimberlites, which is consistent with the petrological observations.

1. Introduction

Kimberlites are heterogeneous rocks, with variable contents of groundmass minerals, xenocrysts and xenoliths entrained by the magmas during their ascent towards the surface (Mitchell, 1986). As a consequence of their complex nature, dating kimberlites and characterising their source are challenging. Bulk-rock analyses cannot be used to constrain either the age of the kimberlite eruption or the isotopic signature of the original magma, since each rock represents a compositional spectrum resulting from a mixture of crystals and liquids of diverse origin (e.g. Paton et al., 2007; Donnelly et al., 2012). Crustal contamination and post-emplacement alteration also can have significant effects on the bulk-rock data (Le Roex et al., 2003; Kjarsgaard et al., 2009), further complicating the understanding of kimberlite petrogenesis. These problems, coupled with the improvement of the in situ methods and incorporation of LA-ICP-MS as a routine technique, have led to an increasing interest in the geochemical and isotopic analysis of groundmass minerals as the best approach to characterise these rocks.

Angola is ranked fourth in Africa in terms of kimberlite abundances (Faure, 2010), but very little dating work has been carried out. A summary of published ages for Angolan kimberlites is given in Table 1, including the method used to constrain the time of eruption of each pipe. Almost all the ages have been obtained by U–Pb dating of zircon (Davis, 1977; Haggerty et al., 1983; Eley et al., 2008; Robles-Cruz et al., 2012). However, since zircon is always a xenocryst in the kimberlitic rocks, the measured age may pre-date the eruptive event, leading to misinterpretation of the links between kimberlite eruption and tectonic events. A few studies have been carried out to date kimberlite emplacement through direct analysis of groundmass minerals such as phlogopite (Creaser et al., 2004; Egorov et al., 2007; Tappe et al., 2014). However, in the Angolan kimberlites studied here, phlogopite is

* Corresponding author at: Department de Cristal·lografia, Mineralogia i Dipòsits Minerals, Universitat de Barcelona, Martí i Franquès s/n, 08028 Barcelona, Catalonia, Spain.
E-mail address: montgarri.castillo-oliver@students.mq.edu.au (M. Castillo-Oliver).

http://dx.doi.org/10.1016/j.chemgeo.2015.12.014
0009-2541/

Table 1
Summary of published Angolan kimberlite eruptions.

Kimberlite	Age	Author	Method
Alto Cuilo 1	145.1 ± 4	Eley et al. (2008)	U–Pb perovskite
Alto Cuilo 139	135.7 ± 2.1	Eley et al. (2008)	U–Pb perovskite
Alto Cuilo 197	113 ± 0.8	Eley et al. (2008)	U–Pb zircon
Alto Cuilo 254	115.5 ± 1.1	Eley et al. (2008)	Rb–Sr phlogopite
Alto Cuilo 55	113 ± 0.8	Eley et al. (2008)	U–Pb zircon
Catoca	117.9 ± 0.7	Robles-Cruz et al. (2012)	U–Pb zircon
Chicuatite	372 ± 8	Egorov et al. (2007)	K–Ar phlogopite
Tchiuzo	121.2 ± 1	Robles-Cruz et al. (2012)	U–Pb zircon
Val do Queve	134 ± 2	Davis (1977)	U–Pb zircon
Val do Queve	133.4 ± 11.5	Haggerty et al. (1983)	Fission track zircon

relatively scarce and it is usually altered by post-emplacement processes. Therefore, dating of phlogopite would not be reliable and more suitable groundmass minerals should be considered.

Over the last decade, perovskite ($CaTiO_3$) has become widely used for both age determination and characterisation of the source of kimberlitic magmas. Perovskite is a ubiquitous minor phase (<10%) in kimberlites and crystallises directly from the magma (Mitchell, 1986). It also is relatively resistant to weathering (Heaman, 1989) and a main carrier of U (>100 ppm) and Th (Heaman, 1989). Thus in situ LA-ICP-MS (laser ablation inductively coupled plasma mass spectrometry) U–Pb analysis of perovskite has turned out to be an excellent means to date the eruption of kimberlites (e.g. Batumike et al., 2008; Donnelly et al., 2012; Sun et al., 2014), lamprophyres and melilitites (Tappe et al., 2006; Corfu and Dahlgren, 2008) and carbonatites (Cox and Wilton, 2006; Reguir et al., 2010). This technique has some advantages over other instruments such as SIMS (e.g. Smith et al., 1989) and ID-TIMS (Heaman, 1989), since it is rapid, cost-efficient and allows spatial control on the analysed grains. However, to the authors' knowledge, in Angola only two pipes, from the Alto Cuilo kimberlite field, have been dated through U–Pb analysis of perovskite (Eley et al., 2008), and the paper did not specify which technique was used to obtain these data.

In addition to its potential for U–Pb dating, Heaman (1989) envisaged that perovskite could also be used to assess the origin of the kimberlite magma based on Sr and Nd isotope studies. Perovskite usually has high Sr and low Rb contents, which leads to very low $^{87}Rb/^{86}Sr$ ratios (<0.001). Therefore, it is an ideal mineral for Sr isotope studies because Sr_i is insensitive to any age correction (Heaman, 1989; Paton et al., 2007). The use of groundmass perovskite therefore represents an improvement, in terms of constraining possible mantle reservoirs of the kimberlites, over the values obtained from bulk-rock analyses, whose Sr–Nd isotopic signature is known to be modified by crustal contamination (e.g. Paton et al., 2007; Donnelly et al., 2012; Tappe et al., 2012; Chalapathi Rao et al., 2013; Sarkar et al., 2014).

Here we present the first work of in situ U–Pb geochronology and Sr–Nd isotope analysis of perovskite grains from Angolan kimberlites, based on a detailed petrographic and chemical study of this mineral from six pipes. These results can provide key information on the tectonic evolution of the Lundas kimberlitic province in Early Cretaceous time, which is still poorly understood, and also contribute to our knowledge of the sources of the Angolan kimberlites.

2. Geological setting

Angola is located in the south-western part of the Congo-Kasai Craton, which occupies a large part of central Africa, extending from Sudan through the Democratic Republic of Congo to Angola. The Congo-Kasai Craton was formed and stabilised during the Mesoarchean (Pereira et al., 2003 and references therein). Subsequently three main orogenic cycles defined the geology of the country: the Eburnean (2–2.2 Ga), the Kibaran (1.4–1 Ga) and the Pan-African (590 Ma). The Eburnean event was the most important one, deforming most of the rocks of the country, while the effects of the Kibarian and Pan-African orogenies were of more local scale (Pereira et al., 2003). Finally, during the break-up of Gondwana (190–60 Ma) thick sedimentary sequences were deposited in the basins created as a result of this extension (Pereira et al., 2003).

As shown in Fig. 1, most of the kimberlites and carbonatites found in Angola are located in the Lucapa corridor, which crosses the country from NE to SW. This major extensional structure can be traced for more than 1600 km across the Congo Craton into the Democratic Republic of the Congo (Reis, 1972) and continues to the southwest to the transforms of the Mid-Atlantic Ridge with 300 km dextral offsets (Reis, 1972; Sykes, 1978).

Four kimberlite and carbonatite provinces (I–IV) can be distinguished within this structure. Province I, on the north-eastern area of the Lucapa Corridor, represents the main Angolan kimberlite field. There is an increase in the number of carbonatite intrusions from northeast to southwest; province IV is mainly carbonatitic and contains very few diamondiferous kimberlites (White et al., 1995). Two secondary fault systems (ENE–WSW and NNW–SSE) play a major role in kimberlite emplacement in these provinces. However, the E-NE fault-fracture corridors are predominant and are interpreted as R-shears with a dextral sense of displacement (White et al., 1995). These corridors are particularly important in Provinces I and IV, whereas kimberlite emplacement in Provinces II and III is thought to be mostly controlled by the intersection of the conjugate (NW–NNW) corridors (R′-shears) with the Lucapa Corridor (De Boorder, 1982).

In Angola, the erosion rate of the sedimentary cover is extremely low compared to other cratonic areas worldwide (Hawthorne, 1975; Pervov et al., 2011). Therefore, the diatreme and hypabyssal facies, where perovskite is expected to be better preserved, are rarely reached during the drilling work done at the exploration stage. As a consequence, only six out of 25 kimberlites sampled are included in this study. The diamond grade has only been assessed for the Cat115, Lucapa 1 and Lucapa 2 kimberlites, the first two being diamondiferous and the latter, barren. All these kimberlites are located in the Lunda Norte area (Fig. 1). Like most kimberlites from Province I, their emplacement is mainly controlled by fault-bounded compartments with WSW–ENE direction which are dislocated by NNW–SSE faults, giving an en-echelon pattern (Pereira et al., 2003).

3. Methods

Kimberlite samples were obtained from drill-cores provided by the CATOCA Company. Sample preparation was subsequently conducted at the Thin Section Service of the Universitat de Barcelona. Each sample was sawed into slices and those showing the least alteration and the lowest abundance of xenoliths were selected. This material was then prepared either as thick (100 μm) polished sections or as polished blocks set in 25 mm epoxy mounts.

3.1. Major- and trace-element analysis

Two different electron microscopes (SEM Leica Cambridge S.36 and ESEM Quanta 200 FEI XTE 325/D8395) in the Centres Científics i Tecnològics (CCiT) of the Universitat de Barcelona (UB) were used for the characterisation of the textures, alteration and zoning patterns of the perovskite grains. A focused beam with an accelerating voltage of 20 keV was used.

Major-element and Nb, La and Ce contents were analysed with a CAMECA SX50 electron microprobe with four wavelength-dispersive spectrometers (WDS), in the CCiT-UB. The approximate diameter of the electron beam was 1–2 μm. Analytical conditions were 20 KeV accelerating potential, a beam current of 10 nA and a take off angle of 40°. Both for major and minor elements, counting times were 10 s for the peak and 10 s for the background. Standards used for calibration are the following: Na (Kα, TAP, albite), Al (Kα, TAP, corundum), Si

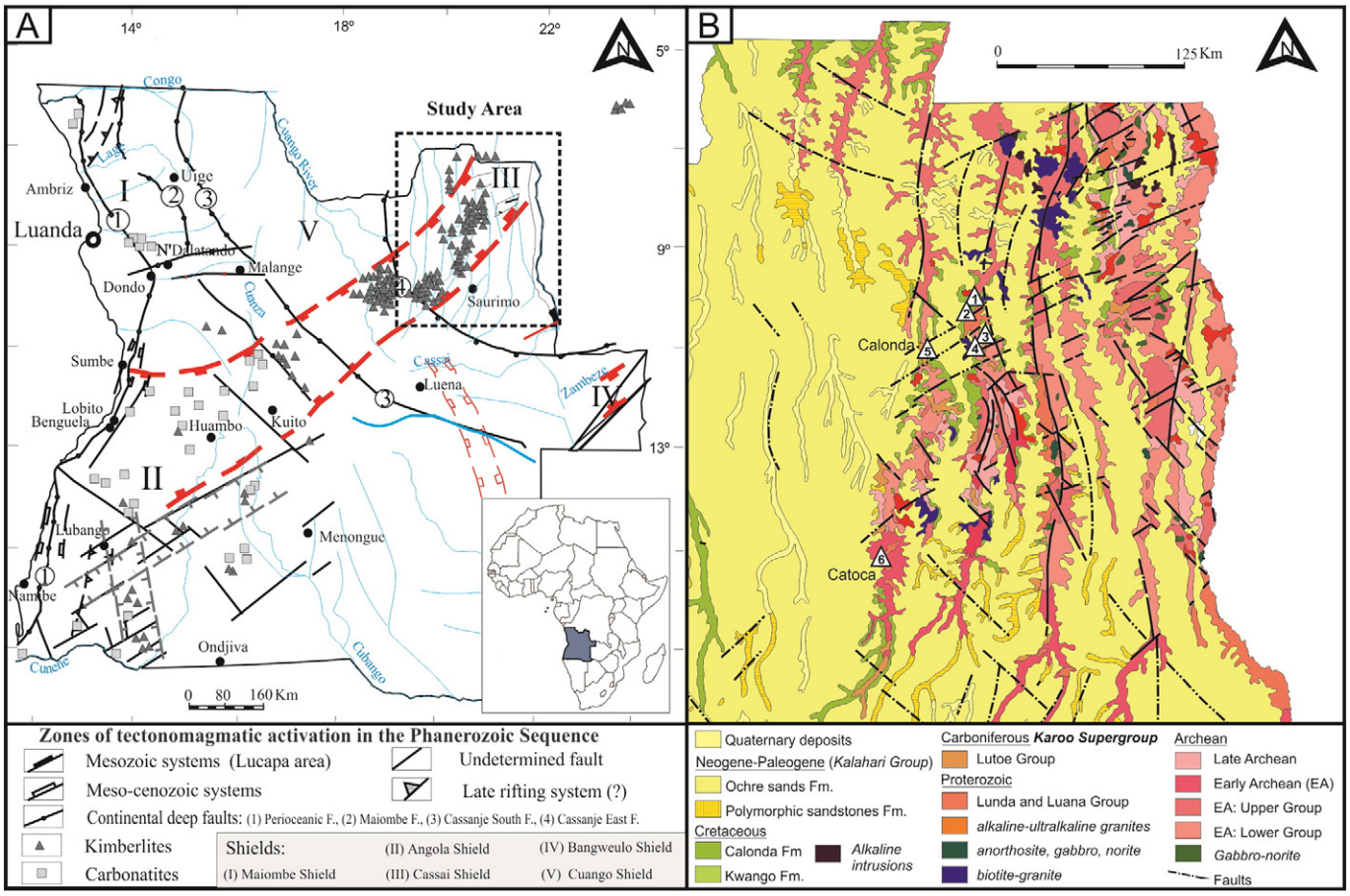

Fig. 1. (A) Structural map of Angola. (B) Detailed geological map of the study area, showing the location of the six studied kimberlites: (1–2) Mulepe; (3–4) Lucapa; (5) Calonda and (6) Cat115 kimberlites (modified from Perevalov et al. (1992), Guiraud et al. (2005), Egorov et al. (2007) and Robles-Cruz et al. (2012)).

(Kα, TAP, diopside), K (Lα, PET, orthoclase), Ca (Kα, PET, wollastonite), Ti (Kα, PET, rutile), Fe (Kα, LiF, Fe_2O_3), Sr (Lα, PET, celestine), Nb (Lα, PET, Nb^0), La (Lα, PET, LaB_6), Ce (Lα, PET, CeO_2), Nd (Lα, LiF, REE4) and Ta (Lα, LiF, Ta^0). Totals between 99 and 101% were accepted. The raw data were corrected using the Pouchou and Pichoir (1984) reduction.

Trace elements (Na, Mg, K, Sc, V, Fe, Rb, Sr, Y, Zr, Nb, Ba, REE, Hf, Ta, Th, U and Pb) of perovskite grains were analysed on polished sections >100 μm thick and on polished mounts using a New Wave Research UP-213 laser ablation microsampling system attached to an Agilent 7700cx 300 ICP-MS at the GAU (Macquarie University). For calibration the NIST 610 glass was used and each analysis was normalised using the Ca values determined by the electron microprobe. Samples were analysed in runs of 16 analyses comprising 12 analyses of unknowns bracketed by two analyses of the standard at the beginning and end of each run. Additionally, one analysis of the USGS BCR-2 standard was included in each run as a secondary standard to monitor the accuracy of the measurements. The ablation or total counting time for each analysis was 120 s. Typical detection limits range from 5 to 50 ppb for V, Rb, Sr, Y, Zr, Nb, REE, Hf, Ta, Th, U and Pb, 100 ppb for Ba and Sc and <1 ppm for Na and Mg. The relative precision and accuracy for a laser microprobe analysis range from 1 to 10%. The spot size ranged between 15 and 40 μm. As a result, given the small size of the perovskite grains, only one spot was analysed on each grain.

3.2. In situ U–Pb dating using LA-ICP-MS

Determination of U–Pb ratios was done following the methods described by Batumike et al. (2008) for U–Pb dating of kimberlites from the Congo Republic. The analyses were performed using a New Wave Research UP-213 laser ablation microsampling system coupled to an Agilent 7500 ICP-MS system at GEMOC (Macquarie University). Measurements of U–Pb were done in situ on thick (100 μm) polished sections and polished blocks, using a spot size ranging from 30 to 40 μm. Each analytical run consisted of 8–12 analyses of unknowns, bracketed by two analyses of a primary standard (zircon GJ-1, 609 Ma) at the beginning and the end of each run. Additionally, two near-concordant zircons (91,500, 1065 Ma, (Wiedenbeck et al., 1995); Mud Tank, 732 ± 5 Ma, (Black and Gulson, 1978)) were analysed as secondary standards after the first two GJ-1 analyses in order to assess the accuracy and precision of the method. As already suggested by Storey et al. (2007) for titanite, and demonstrated by Batumike et al. (2008) for perovskite, strict matrix matching of the sample and the external standard is not essential for U–Pb dating by LA-ICP-MS. Typical acquisitions consisted of 60 s background measurement followed by 120 s of sample ablation. The ablation was done in He instead of Ar, since it leads to efficient sample transport, signal stability and better reproducibility of U/Pb fractionation. The laser was set to give a 2.5 mJ/cm^2 energy, using 5 Hz repetition rate for all the analyses. Avoidance of cracks and inclusions was achieved by selecting the stable parts of the ablation signal, with data collected in time-resolved mode. This also enabled termination of the analysis if the laser drilled into the kimberlite matrix.

The U–Pb isotope ratios were obtained from raw signals using the software programme GLITTER (Griffin et al., 2008). The common-Pb correction was done using a regression technique, as described by Batumike et al. (2008). The upper intercept of the regression line defined by the raw data on a Tera–Wasserburg plot is taken as the $^{207}Pb/^{206}Pb$ of the common-Pb component. The lower intercept gives the crystallisation age of the perovskite population, and hence the

kimberlite. The slight scatter observed in some of the data may reflect heterogeneity in the composition of the common-Pb component due to intrinsic variations of the Pb composition of the mantle. Pb loss can also occur in highly altered perovskites (Donnelly et al., 2012), giving unrealistically young ages. However, as discussed later, these problematic ages can be identified by anchoring the upper intercept to the present-day $^{207}Pb/^{206}Pb$ terrestrial value. Therefore, the points that did not fit the initial correlation line within 1σ have been rejected in order to reduce the scatter of the data. The U–Pb plots and the regression calculations were done using the Isoplot 4.0 software of Ludwig (2003).

3.3. In situ Sr–Nd analyses by LA-MC-ICP-MS

The Sr–Nd isotopic analyses were conducted at the GEMOC laboratories (Macquarie University, Sydney) using a Nu Plasma MC-ICP-MS attached to a New Wave Research UP-213 laser ablation microsampling system. The detailed analytical procedure followed in this study can be found in Donnelly et al. (2012) and only a brief summary of the protocol is given here.

The laser was set to produce 30–50 μm diameter spots, with 5 Hz repetition rate, and a fluence of 2.5 mJ/cm^2. Due to the small grain size of most of the perovskite crystals, only one analysis could be performed on each grain. Therefore, in this work the Nd–Sr isotope study has been carried out under the premise that all the perovskite grains of the same kimberlite were derived from the same source.

As in the U–Pb analyses, a time-resolved software was used in order to select the more stable portions of the ablation signal, giving only the data strictly corresponding to perovskite and excluding contributions to the signal from inclusions, cracks or other phases.

The Nd isotopic data were acquired in static mode, measuring masses 142, 143, 144, 145, 146, 147, 148 and 150 simultaneously in Faraday collectors. To calibrate the instrument, as well as to monitor the reproducibility and evaluate the accuracy of the data, a standard 100 ppb JMC321 Nd solution was used. Corrections for mass fractionation and the interference of ^{144}Sm on ^{144}Nd were made following the method described by Donnelly et al. (2012).

For the in situ Sr-isotope analyses, masses 83, 83.5, 84, 85, 85.5, 86, 86.5, 87 and 88, were measured simultaneously in Faraday collectors, in static mode. The interferences of ^{86}Kr on ^{86}Sr and doubly charged REE on the isotopes of interest, as well as the mass fractionation, were also corrected using the procedures given by Donnelly et al. (2012). No ^{87}Rb correction on ^{87}Sr was applied, in order to avoid overcorrection of the initial $^{87}Sr/^{86}Sr$ ratios, which would result from the very low Rb contents (close to the detection limit, and consequently with high uncertainties) of the analysed perovskite grains.

In order to verify the accuracy and external precision of the in situ LA-MC-ICP-MS data for both Nd and Sr, repeated measurements of the Ice River perovskite ($^{143}Nd/^{144}Nd = 0.512598 \pm 49$; $^{87}Sr/^{86}Sr = 0.702870 \pm 130$; 2σ uncertainties; n = 57 and n = 69, respectively) were carried out. These results are in good agreement with the values obtained by solution of the same standard ($^{143}Nd/^{144}Nd = 0.512581 \pm 32$; $^{87}Sr/^{86}Sr = 0.702838 \pm 51$; 2σ uncertainties; Tappe and Simonetti, 2012). Since in that work the isobaric interferences for Nd were negligible, the consistency between our measurements and their data for the same standard proves the adequacy of the interference corrections applied here to the LA-ICP-MS data. A total of 71 and 76 perovskite crystals were analysed for Nd and Sr, respectively.

4. Sample description

4.1. Occurrence

Perovskite represents up to 2% by volume of the studied rocks. With the exception of the samples taken from the Cat115 kimberlite, which are volcanoclastic, all the studied rocks were classified as coherent, serpentinized, macrocrystic olivine kimberlites. They are composed partly of rounded olivine crystals (20–35% volume) totally replaced by serpentine. The interstitial medium is mainly composed of serpentine, with variable amounts of calcite, ilmenite, phlogopite, spinel, apatite and sulphides. Perovskite belongs to the groundmass minerals and it occurs as primary euhedral, subhedral or rounded crystals scattered in the fine-grained matrix of the kimberlite. Based on textural observations two main textural types of perovskite may be defined: i) primary and ii) secondary.

4.1.1. Primary perovskite

This is the most common perovskite type and is present in all the studied kimberlites. This type of perovskite occurs as discrete single crystals, and can be interpreted as a primary phase crystallising directly from the magma. Two subtypes can be distinguished, based on the perfection of the crystals, their zoning pattern and the presence/absence of inclusions.

4.1.1.1. Anhedral perovskite. Crystals are rounded to sub-rounded and grain size typically ranges from 10 to 60 μm. The only exception are the Calonda perovskites, which are mostly euhedral and commonly smaller (<20 μm). They are usually scattered in the serpentinised groundmass of the kimberlite, together with calcite and apatite, as well as with some xenocrysts such as ilmenite and garnet. In some kimberlites, it can form "necklaces" around earlier-formed macrocrysts or phenocrysts of olivine, now replaced by serpentine (Fig. 2a–e). This texture has been described in kimberlites from different geological settings (e.g. Chakhmouradian and Mitchell, 2000; Donnelly et al., 2012). A few crystals contain inclusions of unidentified phases. Anhedral groundmass perovskite typically exhibits a slight zoning, with bright cores and darker rims under backscatter electron (BSE) imaging on the SEM. Perovskite from this group can be partially altered, developing rims of TiO_2 and titanite.

4.1.1.2. Euhedral perovskite. In this work, this type of perovskite is found exclusively in the Mulepe kimberlites, forming small groundmass crystals (up to 30 μm). As shown in Fig. 2(g–i) they are always euhedral in shape, giving diamond or hexagonal sections with straight boundaries. Commonly they show neither replacement nor alteration to other minerals. This group usually has inclusions, which may be from <0.5 to 10 μm in diameter. The smallest inclusions are usually located near the grain boundaries, whereas the largest inclusions, when present, commonly occupy the centre of the grain. The latter could be identified as serpentinised olivine and apatite. Most of the crystals show a distinctive oscillatory zoning pattern in BSE images, which has not been reported in the other types of perovskite described here.

4.1.2. Secondary perovskite

4.1.2.1. Reaction-induced rims on ilmenite. In some kimberlites, perovskite is found as reaction-induced rims on earlier-crystallised Ti-bearing oxides belonging to the macrocryst suite, mainly Mg-ilmenite (Fig. 2j–l). This texture was described by Boctor and Boyd (1981), and it is interpreted as the result of interaction between ilmenite and the kimberlite magma (Chakhmouradian and Mitchell, 2000). Some of these ilmenite xenocrysts were altered to ulvöspinel before being coated by perovskite. The thickness of this coating ranges from few microns up to 15 μm in rare cases. Large (25–30 μm on average) and rounded crystals of perovskite commonly crystallised around the ilmenite xenocryst. A normal zoning pattern, defined by decrease in Na, Nb and LREE from core to rim, can be recognised in a few of these grains, which always remain unaltered. The presence of ilmenite inclusions is not unusual in this type of perovskite.

4.1.2.2. Nb-rich perovskite overgrowths. Some significantly larger (>100 μm) groundmass grains (Ia perovskite) in the Mulepe 2

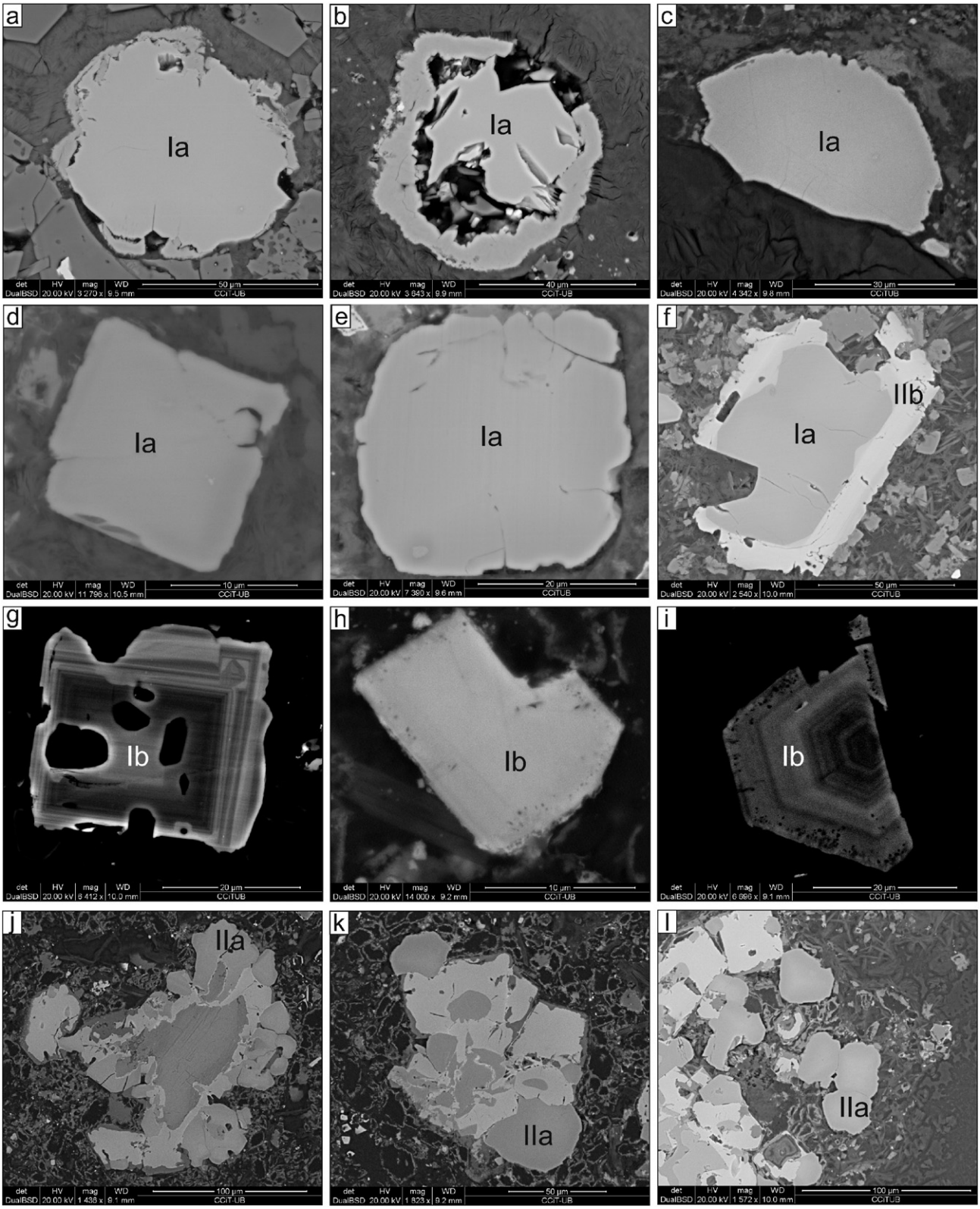

Fig. 2. Back-scattered electron (BSE) images of perovskite showing the different textural types found in the studied kimberlites. (a) groundmass perovskite (Lucapa 1); (b) highly altered groundmass perovskite, with TiO_2 rim (Lucapa 2); (c) groundmass perovskite as necklace around serpentinised olivine xenocryst (Cat115); (d) euhedral groundmass perovskite (Calonda); (e) subrounded groundmass perovskite (Mulepe 1); (f) groundmass perovskite with a Fe–Nb rich perovskite overgrowth (Mulepe 2); (g–i) euhedral perovskite with strong oscillatory zoning and inclusions and (j–l) reaction-induced rims of perovskite on ilmenite xenocrysts (Calonda and Mulepe kimberlites).

kimberlite characteristically are overgrown by Nb-rich perovskite (up to 10.6 wt% Nb_2O_5) with sharp boundaries between the original grain and the late generation of perovskite (Fig. 2f). A similar overgrowth has also been described in Canadian and South African kimberlites (Chakhmouradian and Mitchell, 2001; Donnelly et al., 2012).

4.2. Alteration

Resorption, cation leaching and replacement of perovskite by other minerals are common processes in hypabyssal and diatreme facies kimberlites (Chakhmouradian and Mitchell, 2000). Perovskite is unstable in a CO_2-rich, weakly acidic environment (Chakhmouradian and Mitchell, 1998). As a result, during the final stages of kimberlite evolution, perovskite is commonly replaced by other Ti-bearing minerals. In the kimberlites studied here, titanium dioxide (TiO_2) is the most common alteration product. It appears in the CAT115 kimberlite, as well as in both barren and diamondiferous kimberlites from Lucapa. The formation of TiO_2 at the expense of perovskite involves the crystallisation of calcite by leaching of Ca (Chakhmouradian and Mitchell, 2000). As shown in Fig. 2b, this gives the TiO_2 rim a characteristic "spongy" appearance. In some cases, an atoll shape, similar to that observed in groundmass spinel, was recognised.

In the Cat115 kimberlite, perovskite has been replaced by titanite, which has been previously interpreted as an indicator of higher SiO_2 activity in the later stages of the crystallisation due to either crustal contamination (Chakhmouradian and Mitchell, 2000) or magma cooling (Carmichael et al., 1970). No rims of late Mn–Nb-rich ilmenite have been found on any of the perovskite grains.

5. Major-element composition

Most of the perovskite analyses are close to the ideal composition ($CaTiO_3$), with lesser concentrations of LREE, Na, Sr, Nd, Al, Fe, Nb and Ta. Negative correlations of Ce, La, Nd, Nb and Na against Ca and Ti

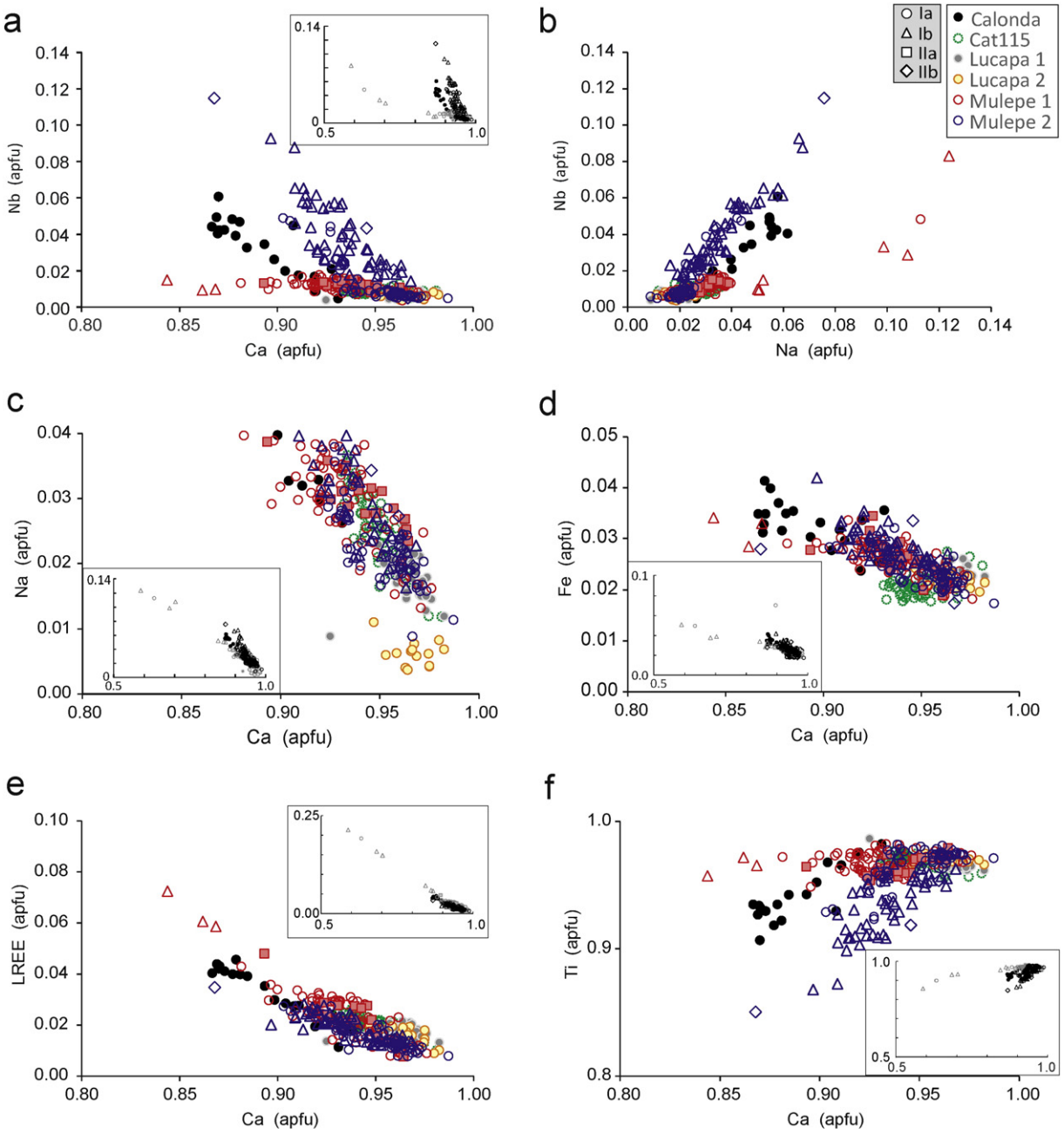

Fig. 3. Binary diagrams representing the major-element chemistry of the perovskites, in atoms per formula unit (apfu). Symbols correspond to the different perovskite textures found in the kimberlites: subtype Ia (circles), subtype Ib (triangles), subtype IIa (squares) and subtype IIb (diamonds). The kimberlitic bodies are represented by different colours and lines (see legend in Fig. 3b). Calcium is represented against Nb (a), Na (c), Fe (d), REE (e) and Ti (f). The Na–Nb (b) diagram shows a positive correlation and significantly higher Na and Nb contents in subtype Ib perovskite. Conversely, a negative correlation is found between Ca and Nb, Na, REE and Fe.

have been observed (Fig. 3a–f). Na and Nb correlate positively in all the analysed grains (Fig. 3b), particularly significant in the Mulepe kimberlites, in which perovskite is more enriched in the lueshite component ($NaNbO_3$).

Based on their major-element compositions, three different groups are distinguished, as shown in the bivariate diagrams in Fig. 3. Table 2 summarises the textures and compositions typical of the studied Angolan kimberlites, whereas the average compositions of each group and for each kimberlite are reported in Table 3. Major-element composition of the whole dataset can be found in the supplementary file 1.

5.1. Group 1

All the studied kimberlites contain this compositional group, which occurs both as groundmass perovskite (type Ia) and reaction-induced rims on ilmenite (type II). This is compositionally homogeneous and it is characterised by relatively low average contents of REE (mean 1.0 wt% ΣLREE) and Nb (0.4–4.6 wt% Nb_2O_5), and by low Na contents (0–1.0 wt% Na_2O). These values are in good agreement with those found in perovskite II as defined by Chakhmouradian and Mitchell (2001) in Canadian kimberlites. However, groundmass perovskite from Calonda kimberlite is enriched in these elements (mean 3.3 wt% ΣLREE and up to 5.7 wt% Nb_2O_5 and 1.3 wt% Na_2O).

5.2. Group 2

Only the Mulepe kimberlites contain this compositional group and it corresponds to type Ib perovskite, usually showing very strong zoning. This is significantly enriched in La, Ce and Nd (up to 22.5 wt% ΣLREE). Niobium (0.9–8.8 wt% Nb_2O_5) and sodium (0.4–2.4 wt% Na_2O) contents are also high compared to most of the grains from group I perovskite, thus indicating a high abundance of the lueshite component. However, due to its low content of Zr (165–2824 ppm) this perovskite type cannot be equated with the perovskite III group defined by Chakhmouradian and Mitchell (2001). Similar enrichments in LREE, Nb and Na in late crystallising perovskites have been observed in a wide range of alkaline-ultramafic and carbonatitic rocks (Platt, 1994; Chakhmouradian and Mitchell, 1998).

5.3. Group 3

In addition to these two main compositional groups, a third distinctively different composition is defined by the Nb-rich overgrowth on some perovskite crystals from the Mulepe 2 kimberlite. These rims have very high Nb contents (up to 10.6 wt% Nb_2O_5), with only a slight enrichment of other minor elements such as LREE (1.8–4.0 wt% ΣLREE) or Na (0.8–1.6 wt% Na_2O).

Zoning is a very common feature in perovskite grains from kimberlites worldwide. Chakhmouradian and Mitchell (2000) defined the *normal pattern* as a decrease in LREE and Th in the outer part of the crystal, which may or may not be accompanied by a decrease in Na and Nb contents. These authors also found that it can be complicated by the presence of transitional zones characterised by intermediate LREE contents. Most of the perovskite grains from the kimberlites studied here exhibit this pattern, with a bright core and a darker rim in BSE images (Fig. 4a), related to a decrease in Na, Nb and LREE towards the rim. The *reverse pattern*, with enrichment in LREE and Th towards the rim, is rare in perovskite crystallised from kimberlitic magmas. In the Angolan kimberlites this pattern is found only occasionally in type Ia perovskites and it is characterised by an increase in the Fe and Nb contents, although the LREE values remain constant or decrease slightly (Fig. 4b). The reverse zoning has been previously interpreted as the result of a re-equilibration of the perovskite with a magma that has been compositionally modified by assimilation or contamination processes. *Oscillatory zoning* is quite rare in kimberlites worldwide and it typically reflects variation in Ca, Ti and LREE contents (Chakhmouradian and Mitchell, 2000). However, the oscillatory pattern (Fig. 4c-h) is very common in type Ib perovskite from the Mulepe samples and it is defined by significant variations in Nb, Na, Ce, Fe and Nd within a single grain. As shown in Fig. 4h, the brighter areas of the BSE images of this zoning have the highest LREE (11.9–20.3 wt% LREE), Sr (0.5–1.5 wt% Sr_2O), Na (1.6–2.2 wt% Na_2O) and Nb (1.1–7.0 wt% Nb_2O_5) contents, while the darkest zones show lower contents of these elements but still higher than group 1 perovskite (1.4–8.3 wt% LREE oxides, 0–0.6 wt% Sr_2O, 0.4–1.5 wt% Na_2O) with slightly higher Nb contents (0.9–8.8 Nb_2O_5 wt%).

6. Trace-element composition

The complete set of trace-element compositions of the perovskites is included in Supplementary file 2. The chondrite REE normalised patterns (Fig. 5) have smooth negative slopes, reflecting the enrichment in LREE with respect to the MREE and HREE (La_N: 4350–7850 vs Lu_N: 8–12). This diagram also confirms that perovskite is a main carrier for REE and high field strength elements (Zr, Hf, Nb, Th and U). In contrast, perovskite is extremely depleted in Rb (usually <0.8 ppm or below detection limit), Ba, K and Sc with respect to the whole rock kimberlite composition, with compositions close to the chondritic values. As already observed by Chakhmouradian et al. (2013) and Beyer et al. (2013), perovskite shows higher affinity for Th, Ta, Hf, Ho and LREE relative to U, Nb, Zr, Y and HREE respectively. All perovskite types show a slight negative Y anomaly, giving strongly subchondritic Y/Ho ratios.

Despite the strong enrichment in La and Ce observed in EMP analyses of the bright areas of group II perovskite, both types have

Table 2
Main features of each perovskite type, defined by texture, major-element chemistry, zoning pattern, alteration mineral(s) and presence/absence of inclusions. Note that both Mulepe kimberlites contain all perovskite types.

Type	Ia	Ib	IIa	IIb
Texture	Primary, rounded subhedral	Primary, euhedral	Secondary, pseudomorphic after ilmenite	Nb-rich rims of perovskite on type Ia perovskite
Chemistry	Group 1: Low LREE (<5.58 wt% LREE), Na (<0.97, <1.45* wt% Na_2O) and Nb (<4.65; <5.68* wt% Nb_2O_5)	Group 2: High LREE (<25.55 wt% LREE), Na (2.49 wt% Na_2O) and Nb (<8.8 Nb_2O_5)	Group 1: Low LREE (<5.58 wt% LREE), Na (<0.85 wt% Na_2O) and Nb (<1.46 wt% Nb_2O_5)	Group 3: Low LREE (<3.99 wt% LREE), medium Na (<1.65 wt% Na_2O) and high Nb (10.6 wt% Nb_2O_5)
Zoning (core to rim)	*Normal* (decrease in Na, Nb, LREE) *Reverse* (increase in Fe and Nb, constant LREE) *Oscillatory* (very rare)	*Oscillatory* (very common, with main variations in Nb, Ce, Na)	Unzoned, only occasionally *normal* pattern	Unzoned
Alteration	When present: TiO_2, titanite	Very rare	Very rare	none
Inclusions	Rare	Very common (<0.5 μm, in the rims, to 10 μm, mainly serpentinised olivine, chromite)	Ilmenite	none
Location	Cat 115, Calonda*, Mulepe, Lucapa	Mulepe	Calonda, Mulepe	Mulepe

* Calonda kimberlite is characterised by slightly higher contents of LREE, Na and Nb compared to type Ia perovskites found in the other kimberlites.

Table 3
Averaged major-element (wt%) compositions and structural formula of each textural and compositional group in the six studied kimberlites.

Compositional group	Group 1																Group 2				Group 3	
Textural group	Ia												IIa				Ib				IIb*	
Kimberlite	Cat115		Mulepe 1		Mulepe 2		Lucapa 1		Lucapa 2		Calonda		Mulepe 2		Calonda		Mulepe 1		Mulepe 2		Mulepe	
oxides (wt%)	*av.*	1σ	*av.*	1σ	*av.*	1σ	*av.*	1σ	*av.*	1σ	*av.*	1σ	*av.*	1σ	*av.*	1σ	*av.*	1σ	*av.*	1σ	*av.*	1σ
TiO_2	55.91	0.37	55.60	0.76	56.04	1.13	55.86	0.35	56.40	0.17	53.45	1.72	55.63	0.86	56.62	0.43	50.70	4.15	53.56	1.75	49.81	3.66
Al_2O_3	0.26	0.05	0.10	0.03	0.18	0.04	0.20	0.02	0.17	0.03	0.06	0.02	0.08	0.05	0.06	0.01	0.08	0.04	0.12	0.05	0.11	0.02
FeO	1.20	0.13	1.55	0.33	1.36	0.17	1.35	0.10	1.27	0.09	1.84	0.27	1.46	0.23	2.00	0.08	2.00	0.33	1.63	0.20	1.73	0.25
CaO	38.39	0.61	37.61	0.97	38.72	0.92	39.08	0.49	39.48	0.49	35.57	1.30	38.08	1.08	37.57	0.43	28.91	5.54	37.57	0.93	35.84	2.86
SrO	0.12	0.06	0.11	0.07	0.11	0.06	0.12	0.04	0.13	0.05	0.16	0.10	0.14	0.08	0.31	0.04	0.60	0.31	0.16	0.08	0.12	0.13
Na_2O	0.57	0.12	0.67	0.13	0.51	0.13	0.41	0.08	0.42	0.09	1.03	0.22	0.66	0.10	0.63	0.06	1.67	0.63	0.79	0.27	1.20	0.62
Ta_2O_5	0.20	0.13	0.25	0.14	0.17	0.12	0.16	0.12	0.12	0.07	0.23	0.19	0.19	0.18	0.06	0.06	0.15	0.16	0.15	0.16	0.21	0.29
Nb_2O_5	0.86	0.17	1.13	0.26	1.29	1.06	0.62	0.11	0.61	0.19	3.26	1.27	1.13	0.21	0.65	0.27	2.61	2.32	3.70	1.74	7.37	4.59
La_2O_3	0.52	0.09	0.44	0.14	0.19	0.10	0.22	0.07	0.21	0.05	0.75	0.12	0.44	0.29	0.45	0.18	3.38	1.81	0.32	0.10	0.45	0.32
Ce_2O_3	1.88	0.28	1.80	0.46	1.27	0.23	1.35	0.14	1.23	0.23	2.40	0.48	1.70	0.59	1.13	0.54	7.61	3.81	1.46	0.31	1.77	0.71
Nd_2O_5	0.00	–	0.68	0.29	0.54	0.23	0.55	0.18	0.52	0.21	0.96	0.33	0.68	0.26	0.29	0.01	2.04	0.98	0.60	0.21	0.68	0.52
LREE	2.40	0.34	2.82	0.83	1.76	0.54	2.13	0.26	1.95	0.41	3.93	0.98	2.58	1.10	1.86	0.71	13.03	6.58	2.38	0.54	2.89	1.56
Total	99.94	0.49	99.87	0.48	100.20	0.40	99.97	0.51	100.56	0.27	99.64	0.44	100.03	0.56	99.82	0.22	99.81	0.34	100.11	0.45	99.39	0.01
apfu ($O = 3$)																						
Ti	0.97	0.00	0.97	0.01	0.97	0.01	0.97	0.00	0.97	0.00	0.94	0.02	0.97	0.01	0.98	0.00	0.94	0.04	0.93	0.02	0.88	0.05
Al	0.01	0.00	0.00	0.00	0.00	0.00	0.01	0.00	0.00	0.00	0.00	0.00	0.00	0.00	0.00	0.00	0.00	0.00	0.00	0.00	0.00	0.00
Fe	0.02	0.00	0.03	0.01	0.02	0.00	0.02	0.00	0.02	0.00	0.03	0.01	0.03	0.00	0.03	0.00	0.04	0.01	0.03	0.00	0.03	0.00
Ca	0.95	0.01	0.93	0.02	0.95	0.02	0.96	0.01	0.97	0.01	0.89	0.02	0.94	0.02	0.93	0.01	0.76	0.12	0.93	0.02	0.91	0.06
Sr	0.00	0.00	0.00	0.00	0.00	0.00	0.00	0.00	0.00	0.00	0.00	0.00	0.00	0.00	0.00	0.00	0.01	0.00	0.00	0.00	0.00	0.00
Na	0.03	0.01	0.03	0.01	0.02	0.01	0.02	0.00	0.02	0.00	0.05	0.01	0.03	0.00	0.03	0.00	0.08	0.03	0.04	0.01	0.06	0.03
Ta	0.00	0.00	0.00	0.00	0.00	0.00	0.00	0.00	0.00	0.00	0.00	0.00	0.00	0.00	0.00	0.00	0.00	0.00	0.00	0.00	0.00	0.00
Nb	0.01	0.00	0.01	0.00	0.01	0.01	0.01	0.00	0.01	0.00	0.03	0.01	0.01	0.00	0.01	0.00	0.03	0.03	0.04	0.02	0.08	0.05
La	0.00	0.00	0.00	0.00	0.00	0.00	0.00	0.00	0.00	0.00	0.01	0.00	0.00	0.00	0.00	0.00	0.03	0.02	0.00	0.00	0.00	0.00
Ce	0.02	0.00	0.02	0.00	0.01	0.00	0.01	0.00	0.01	0.00	0.02	0.00	0.01	0.01	0.01	0.00	0.07	0.04	0.01	0.00	0.02	0.01
Nd	0.00	0.00	0.00	0.00	0.00	0.00	0.00	0.00	0.00	0.00	0.01	0.00	0.00	0.00	0.00	0.00	0.02	0.01	0.00	0.00	0.01	0.00
LREE	0.02	0.00	0.02	0.01	0.01	0.00	0.02	0.00	0.02	0.00	0.03	0.01	0.02	0.01	0.02	0.01	0.12	0.06	0.02	0.00	0.03	0.01
Cations	2.00	0.00	2.00	0.01	2.00	0.01	2.01	0.01	2.01	0.00	1.99	0.01	2.00	0.00	2.00	0.00	1.98	0.02	2.00	0.00	1.99	0.02

* Only Mulepe 1 and Mulepe 2 kimberlites have IIb subtype

similar REE patterns when analysed by laser ablation techniques. This is because the spot size (>20 μm) makes it impossible to analyse separately each zoning band (<5 μm wide). As a result, the results given by the LA-ICP-MS reflect the average composition of the whole perovskite grain. Besides a significant enrichment in LREE, the main differences between subtype Ia and Ib are in terms of Na, Sr, Zr, Nb and Hf (Table 4, Figs. 5 and 6a). In contrast, Ta, Th and U contents are quite similar in both textural types. Consequently, type Ib perovskites are characterised by higher Nb/Ta and Th/U ratios (Fig. 6b). Perovskite crystallising as reaction rims on ilmenite is significantly enriched in U, Sr and Nd (180 ppm, 460 ppm, 2100 ppm and 6000 ppm, respectively) compared to the other textural types of perovskite (see Table 4), although its REE contents are systematically lower than those of the other types.

Significant differences can be identified in terms of the trace-element compositions of perovskites in the different kimberlites (Table 4 and Fig. 6). Perovskite in the Calonda kimberlite is typically enriched in Nb (mean 16,800 ppm), Zr (mean 1200 ppm), U (mean 370), Th (mean 1260 ppm) and Na (mean 5410 ppm), showing similar compositions to type Ib perovskite from the Mulepe kimberlites. Cat115 kimberlite pipe has also high Zr (up to 1560 ppm) and extremely high Th contents (up to 4520 ppm), which leads to high Th/U ratios (Fig. 6b). Finally each kimberlite field shows a distinctive REE/U ratio, translated into different trends in the REE-U diagram (Fig. 6c).

7. Oxygen fugacity

Major-element contents of perovskite can be used to estimate the oxygen fugacity (fO_2) during kimberlite emplacement. Bellis and Canil (2007) developed an oxybarometer, independent of temperature and bulk composition, based on the Fe and Nb content of perovskite. Since the fO_2 of kimberlite magmas changes during their ascent, the values given by different perovskite generations within a single pipe can shed light on the evolution of this magma from the mantle to the surface. Therefore, this oxybarometer could be useful to unravel not only differences at local or regional scale, by comparing different kimberlites, but also to identify discrete emplacement episodes or magma batches in a single pipe.

As shown in Table 5 and Fig. 7a, most of the type Ia perovskites display a narrow range of Fe and Nb contents, giving a relative fO_2 commonly ranging between ΔNNO −3.0 and −1.0. These fO_2 values are similar to those from other kimberlites worldwide calculated using the same oxybarometer (Fig. 7b). However, the high values reported for the Lac de Gras kimberlites (Canil and Bellis, 2007) were not observed in any of the analysed grains. The results presented here are also consistent with those obtained by the use of other oxybarometers in kimberlites, such as spinel-olivine pairs (Fedortchouk and Canil, 2004; Tappe et al., 2006) and Fe-in-monticellite (Le Pioufle and Canil, 2012) (Fig. 7b), although these yield narrower fO_2 ranges. Oxybarometry of most of type Ib perovskite grains indicates slightly more reducing conditions in the kimberlitic magma from which they crystallised. The large spectrum of ΔNNO observed in this type of perovskite undoubtedly stems from its oscillatory zoning, as well as its strong enrichment in Nb in relation to its medium-low Fe content. Reaction rims of perovskite on ilmenite (type IIa) show relative fO_2 similar to that calculated for groundmass perovskite, but reflect slightly more reducing conditions (ΔNNO down to −4.0) than other perovskite grains in the same kimberlite. In any case, the extremely low values (ΔNNO = −14.9) calculated for Nb-rich overgrowths (type IIb) are unlikely to be real and thus the use of this oxybarometer is not recommended for such compositions. The simplistic approach of this oxybarometer was also mentioned by Chakhmouradian et al. (2013), who considered that it neglects the influence of other highly compatible elements in perovskite (i.e. Ta, REE).

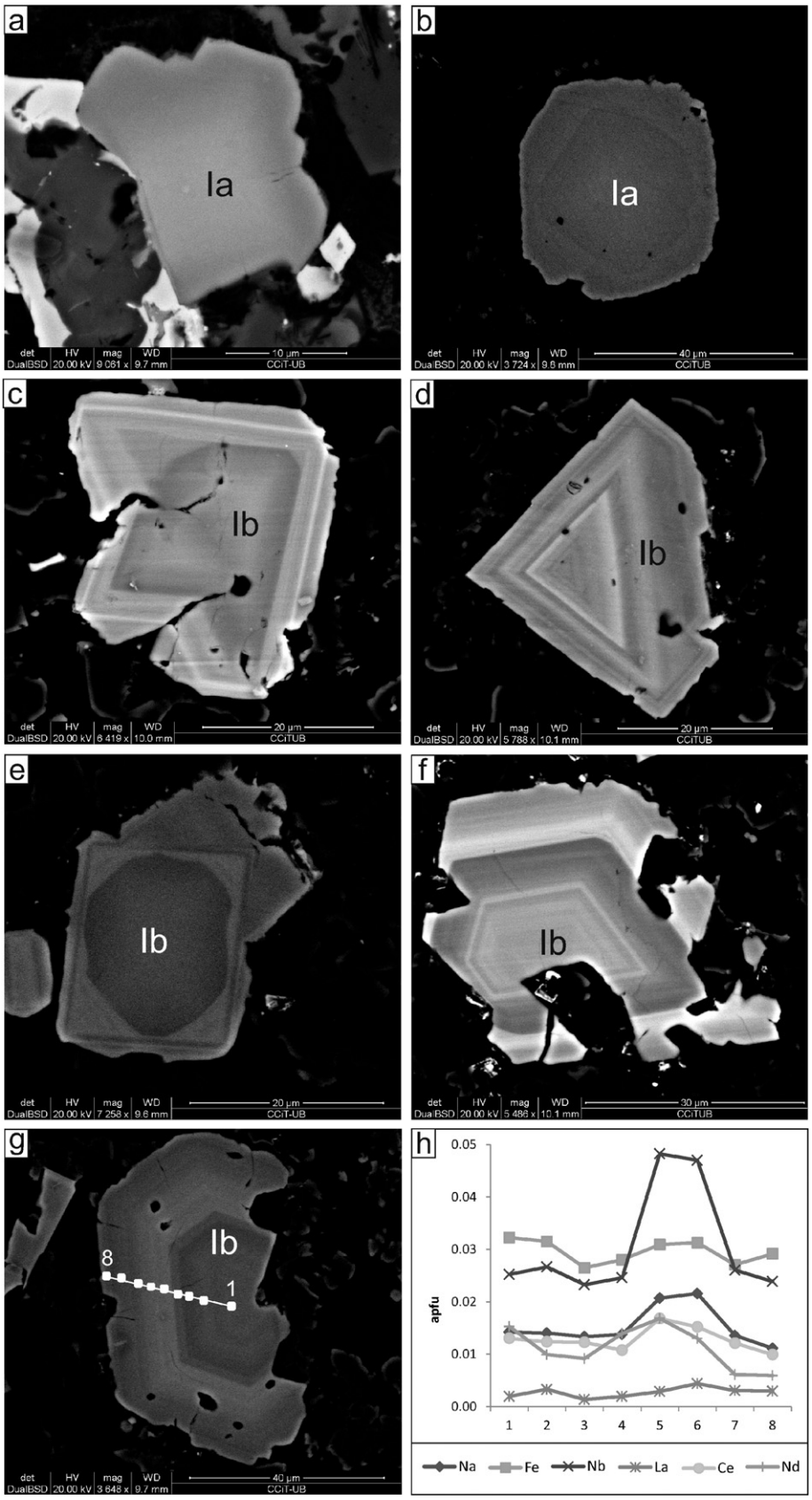

Fig. 4. BSE images of the different zoning pattern found in the studied kimberlites. (a) Normal zoning pattern, with Na- and Nb-poor rim. (b) Inverse zoning pattern, given by a decrease in Fe and Nb rim-wards. (c–g) Complex oscillatory zoning patterns in subtype Ib perovskite from the Mulepe kimberlites. As shown in the major-element profile (h) corresponding to the crystal, the brighter areas are given by higher concentrations of Nb, Na and REE.

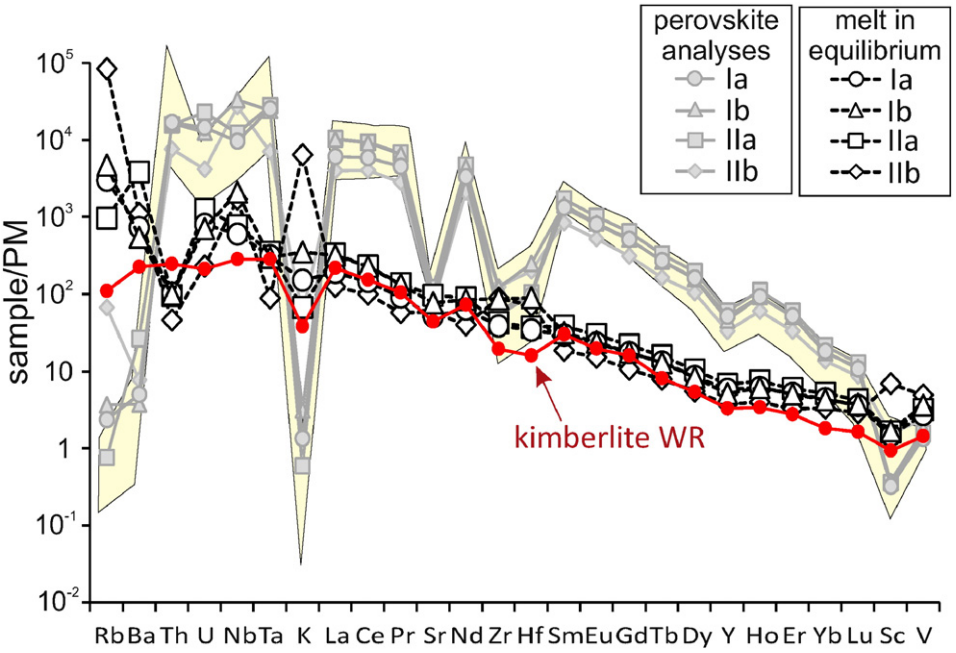

Fig. 5. Average composition of each perovskite textural type normalised to the primitive mantle of McDonough and Sun (1995). The melt in equilibrium for each type of perovskite was calculated from the KD published by Chakhmouradian et al. (2013) and it is discussed further on in this article. The ochre field corresponds to data from perovskite from kimberlites worldwide (Chicken Park; Iron Mountain, Udachnaya and Grizzly kimberlites; from Chakhmouradian et al. (2013). The average whole rock kimberlite (WR) composition has also been taken from Chakhmouradian et al. (2013) calculated from 75 pipes worldwide. Given the small size of the type IIb perovskite, the high Rb, Ba and K values are probably an artefact caused by ablation of phlogopite.

8. U–Pb dating

The complete set of U–Pb dating results is presented in Supplementary file 3 and they are summarised in Table 6. Trace element analyses reveal a significant difference in the U contents of perovskite between Calonda and the other studied kimberlites. Perovskite has very similar U contents (125–730 ppm and 125–680 ppm) in the two kimberlites from Mulepe and these values are very similar to those from Calonda (280–400 ppm). In contrast, kimberlites located near Lucapa have systematically lower values (50–240 U ppm) in perovskite. These differences among the pipes have also been observed in terms of Th content, although in this case the variation within a single kimberlite can also be very important (Mulepe 1 20–2400 ppm; Mulepe 2 15–5150 ppm; Calonda 630–1770 ppm; CAT115 10–4520 ppm; Lucapa 1 230–1580 ppm and Lucapa 2 680–830 ppm).

After common-Pb correction of the LA-ICP-MS datasets, the age of eruption of each kimberlite was calculated using ISOPLOT. The results are presented in Fig. 8. Perovskite analyses on the two Mulepe kimberlites, the Calonda kimberlite and the CAT115 kimberlite yield U–Pb ages identical within error (116.2 ± 6.5 Ma, 123.0 ± 3.6 Ma, 119.5 ± 4.3 Ma and 133 ± 10 Ma, respectively).

Previous work by Yang et al. (2009) and Donnelly et al. (2012) found that alteration of perovskite could produce a spread in U–Pb isotopic composition and give anomalous younger ages as a result of Pb loss. To better constrain the influence of Pb loss on the calculated ages, the composition of the common-Pb component was fixed at the present-day $^{207}Pb/^{206}Pb$ terrestrial value of 0.835722. The same procedure was applied using a value of 0.83110, which is the $^{207}Pb/^{206}Pb$ value of the convecting-mantle source at 240 Ma [both values are calculated from Stacey and Kramers, 1975]. With the exception of the Lucapa kimberlites, the ages from the anchored regression lines coincide with those obtained without anchoring the common-Pb composition, giving the same emplacement ages within the errors. Therefore, the calculated ages probably represent the time of the eruptions and cannot be ascribed to a higher degree of alteration of the perovskite.

The ages calculated for the Lucapa pipes are not reliable, since they turn out to be either too old (Lucapa 1: 155.6 ± 6 Ma) or too young (Lucapa 2: 83.1 ± 4.6 Ma) compared to those obtained when the composition of the common-Pb component was fixed at the actual $^{207}Pb/^{206}Pb$ value (135.7 ± 6.9 Ma and 152 ± 11 Ma, respectively). In the former kimberlite, the low dispersion of the data, coupled with large uncertainties on individual analyses, can explain the low accuracy of the originally calculated age. The Lucapa 2 kimberlite, in turn, does not represent a younger eruptive episode; its age is a consequence of Pb loss during the alteration of perovskite. In an attempt to estimate the possible intrusion age of these kimberlites, a regression line was drawn through the grains with the least Pb loss, using the present-day $^{207}Pb/^{206}Pb$ value (0.83572) as the upper intercept. By comparing the values obtained by SIMS and LA-ICP-MS Donnelly et al. (2012) showed that this approach can give a good approximation to the actual age of the eruption. However, in our case this approach did not give acceptable values, due to the small number of data points having low Pb loss and their high intrinsic errors. We therefore have calculated provisional ages for each kimberlite, using the $^{238}U/^{206}Pb$ and $^{206}Pb/^{207}Pb$ ratios of the least altered perovskite grain in each pipe, regardless of their error (thus it is not possible to determine the age uncertainty). The best estimated age for the Lucapa 1 kimberlite would be 135 Ma, whereas the Lucapa 2 kimberlite would have intruded around 127 Ma. These ages are at least consistent with the few published data on kimberlitic eruptions in the area (Eley et al., 2008; see Table 1).

9. Sr–Nd isotopes

Sr and Nd contents of the perovskites were obtained by laser ablation techniques (mean values: Lucapa 1, 1220 ± 65 ppm Sr and 3820 ± 610 ppm Nd; Mulepe 1, 1450 ± 560 ppm Sr and 4700 ± 2400 ppm Nd; Mulepe 2, 950 ± 210 ppm Sr and 2920 ± 990 ppm Nd; and Cat115, 1250 ± 31 ppm Sr and 4700 ± 1700 ppm Nd). To ensure the best signal quality in the Sr and Nd isotope analyses, only the kimberlites with perovskite completely lacking alteration and >30 μm were characterised (Cat115, Lucapa 1, Mulepe 1 and Mulepe

Table 4
Averaged trace-element (ppm) compositions of the perovskites of the Angolan kimberlites.

Kimberlite	Lucapa 1		Lucapa 2		Mulepe 1						Mulepe 2						Cat115		Calonda	
Type	Ia		Ia		Ia		Ib		IIa		Ia		Ib		IIb		Ia		Ia	
ppm	*av.*	σ	*av.*	σ	*av.*	σ	*av.*	σ	*av.*	σ	*av.*	σ	*av.*	σ	*av.*	σ	*av.*	σ	*av.*	σ
Na	2210	320	2290	120	3600	1300	8490	270	4230	870	2500	1100	4000	1400	5000	2100	3000	1100	5410	200
Mg	3400	6000	2410	780	5200	7400	4170	140	3100	3500	4700	9800	3000	570	37,000	31,000	5400	5900	28,000	11,000
K	101	43	69.2	2.9	170	150	256	8.4	140	120	170	170	320	200	13,500	9400	130	110	2330	920
Sc	4.38	0.57	4.15	0.23	6.93	9.02	5.06	0.22	5.5	1.7	4.39	0.98	5.7	2.1	25	13	13	21	8.0	1.5
V	107.7	5.7	106	3.5	117	28	110.5	3.6	127	16	120	26	142	26	195	36	91	22	125.6	1.2
Fe	8700	3200	7046	35	13,000	14,000	9220	370	11,000	4400	7300	3300	9400	4900	49,000	12,000	8900	3000	19,900	5400
Rb	0.40	0.36	0.10	0.019	0.9	1.4	0.694	0.064	0.55	0.89	0.64	0.84	1.11	0.95	39	22	0.7	1.2	7.77	0.18
Sr	1220	63	1144	28	1450	560	6860	230	2100	1200	950	210	1290	310	1430	630	1250	310	1850	430
Y	222.7	9.1	222.1	2.4	234	46	49.8	1.7	257	32	179	38	213	40	140	45	244	61	277.0	1.4
Zr	490	130	405	21	528	97	950	32	630	120	430	280	1690	760	1265	64	980	440	1204	35
Nb	4510	280	4070	220	6800	2100	12,130	400	8200	1200	6900	6000	29,000	17,000	17,300	4600	6300	1700	16,800	1000
Ba	19	21	8.43	0.25	23	25	30.7	1.4	22	22	12	26	13	16	53	35	9.3	6.3	118	71
La	3190	160	3280	100	4600	2900	31,300	1000	7000	4800	2290	670	3590	570	2507	31	4800	1300	5930	140
Ce	8400	1200	8710	490	11,500	6500	63,100	2000	16,100	8100	6300	2000	10,100	1100	6590	110	11,300	3600	13,780	99
Pr	1000	150	1070	110	1330	740	6320	200	1770	730	760	250	1160	180	700	130	1320	460	1520	100
Nd	3820	610	4050	320	4700	2400	18,010	570	6000	2000	2920	990	4250	760	2570	450	4700	1700	5330	130
Sm	517	67	548	30	590	240	976	32	710	120	400	120	571	90	332	26	610	200	671.0	7.1
Eu	121	15	126.5	2.8	133	45	144.7	4.7	159	18	93	26	133	22	78.6	7.7	138	41	156.3	5.7
Gd	278	27	285.1	9.2	297	95	308	10	351	37	214	58	294	41	166	7.9	310	91	344.50	0.71
Tb	27.1	2.8	28.32	0.13	28.6	8.3	17.2	0.59	32.4	3.4	21.0	5.3	29.3	5.4	15.78	0.93	29.3	8.1	33.9	2.0
Dy	110	12	109.8	3.0	116	30	43.1	1.6	132	14	87	22	124	16	69	13	117	31	137.2	5.7
Ho	13.93	0.90	14.13	0.31	14.5	3.3	4.30	0.18	16.6	2.0	11.1	2.5	16	2	8.8	2.6	14.7	3.8	17.460	0.014
Er	23.5	1.8	22.6	1.3	24.1	5	7.07	0.34	26.3	3.9	18.8	3.9	26.1	3.7	14.2	4.9	24.2	6.2	28.70	0.99
Tm	2.10	0.28	1.936	0.091	2.04	0.41	0.351	0.034	2.3	0.38	1.60	0.33	2.24	0.3	1.26	0.54	2.11	0.54	2.52	0.20
Yb	8.2	1.1	7.72	0.54	8.4	1.6	1.390	0.14	9.4	1.5	10	13	8.8	1.6	5.9	4.1	8.9	2.4	10.1	1.0
Lu	0.74	0.17	0.747	0.013	0.76	0.17	0.1110	0.019	0.86	0.17	0.64	0.16	0.93	0.16	0.58	0.33	0.78	0.21	0.884	0.067
Hf	21.5	2.3	17.3	1.5	24.9	5.7	56.5	2.0	30.0	6.3	20	14	97	59	55.6	7.1	53	23	57.9	9.1
Ta	740	160	752	39	1140	720	1548	50	1110	640	740	380	860	490	260	160	860	410	730	250
Th	790	440	760	100	1800	1500	3270	110	1500	1400	790	600	1150	720	590	250	1400	1200	1260	730
U	185	34	180.2	7.3	400	170	67.5	2.3	460	120	251	92	291	84	83	14	131	46	365	45

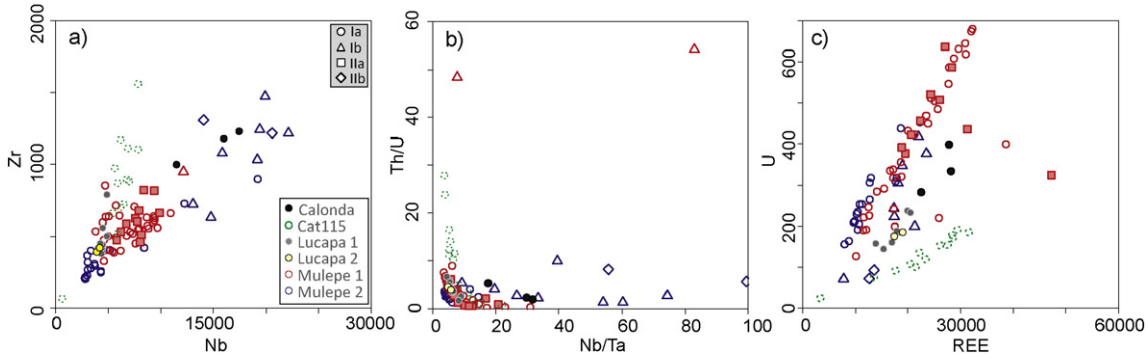

Fig. 6. Selected trace element plots for perovskite of the Angolan kimberlites. (a) Positive correlation between Nb and Zr; (b) Th/U vs Nb/Ta plot and (c) U-REE diagram, showing different U/REE ratios for each kimberlite.

2). For the same reason, type Ib and secondary perovskite from the Mulepe kimberlites were excluded from this study. Despite the aforementioned precautions, large uncertainties and dispersion are still found in the dataset and interpretation should be taken with caution. The small size of the grains, coupled with instability of the instrument during data acquisition, limited the quality of the presented results. A summary of the Sr and Nd isotope compositions is shown in Table 7; the whole dataset and the analyses of the Ice River perovskite are included in Appendixes 4 and 5, respectively.

The $^{87}Sr/^{86}Sr$ ratios in perovskites derived from these four kimberlites overlap, giving isotope compositions identical within their uncertainties: 0.70361 ± 43 (Mulepe 1), 0.70308 ± 31 (Mulepe 2), 0.70323 ± 66 (Lucapa 1) and 0.70405 ± 74 (Cat115). As shown in supplementary files, these values correspond to initial Sr isotopic ratios ranging between 0.70118 and 0.70567. Only analyses with $^{145}Nd/^{144}Nd$ within uncertainty of the canonical value were accepted for further interpretation As seen in Table 7, there is significant dispersion in the $^{143}Nd/^{144}Nd$ values of the remaining dataset, even in perovskite grains derived from the same kimberlite. As a result, large uncertainties are linked to the average $^{143}Nd/^{144}Nd$ perovskite compositions for each pipe: 0.51241 ± 27 (Mulepe 1); 0.51264 ± 8 (Mulepe 2); 0.51270 ± 23 (Lucapa 1) and 0.51265 ± 21 (Cat115). The U–Pb ages of each kimberlite were used in order to obtain an average εNd at the time of the eruption (εNd_i), yielding the following values: $\varepsilon Nd_{116.2} = -2.6 \pm 5.4$ (Mulepe 1), $\varepsilon Nd_{123} = 1.9 \pm 1.6$ (Mulepe 2), $\varepsilon Nd_{135.7} = 3.1 \pm 4.5$ (Lucapa 1) and $\varepsilon Nd_{133} = 2.2 \pm 4.1$ (Cat115).

The $^{87}Sr/^{86}Sr_i - \varepsilon Nd_{(i)}$ diagram (Fig. 9) is conventionally used to distinguish the isotopic reservoirs of the sources of the kimberlites and other mantle magmas (Becker and Le Roex, 2006; Tappe et al., 2011; Donnelly et al., 2012). This figure shows that the average initial Sr and εNd isotopic compositions of 3 out of the 4 analysed kimberlites plot within the Group I kimberlite field, which is consistent with the petrography of the studied pipes. The Mulepe 1 kimberlite shows negative mean εNd values, although the results still plot in the field of Group I kimberlites within the errors.

Table 5
Averaged, minimum and maximum oxygen fugacities of perovskites, calculated using the oxybarometer of Bellis and Canil (2007).

Kimberlite	Type	fO_2			
		av	σ	min	max
Cat115	Ia	−3.4	0.5	−4.3	−1.7
Mulepe 1	Ia	−2.3	0.6	−3.8	−0.6
	Ib	−1.9	1.7	−5.1	−0.5
	IIa	−2.6	0.9	−4.0	−0.4
Mulepe 2	Ia	−3.3	0.9	−6.6	−1.6
	Ib	−5.3	1.9	−10.3[a]	−2.4
	IIb	−9.3[a]	7.9	−14.9[a]	−3.8
Calonda	Ia	−3.5	1.6	−5.9	0.8
Lucapa 1	Ia	−2.4	0.5	−3.2	−0.7
Lucapa 2	Ia	−2.8	0.4	−3.6	−1.8

[a] The unrealistic low fO_2 values are probably an artefact of the high Nb contents.

10. Discussion

10.1. Kimberlite petrogenesis: the Mulepe case

The occurrence of two discrete perovskite populations (type Ia and Ib) in the Mulepe kimberlites, even within the same thin section, suggests that the petrogenesis of these pipes is more complex than for the other kimberlites. As previously shown, these two types of perovskite differ not only in texture (Fig. 2), but also in their major- and trace-element composition (Figs. 3, 5 and 6), their zoning patterns and the presence or absence of inclusions. When considering all these features together, it seems reasonable to suggest that type Ia perovskite was the first population to grow, sometimes developing necklaces around the previously crystallised olivine. Subsequently, a second magma led to the formation of type Ib perovskite, crystallising as discrete grains in the kimberlitic groundmass. The fact that Ib perovskite is typically euhedral and shows no evidences of alteration also supports its late formation, in equilibrium with the last kimberlitic melt. In contrast, type Ia perovskite usually occurs as rounded and partially corroded crystals, indicating partial assimilation as a consequence of its interaction with a late melt under non-equilibrium conditions.

The coexistence of these two completely different populations of perovskite could be either explained by i) reworking of kimberlite facies that underwent different crystallisation processes; ii) degassing of the kimberlite magma or iii) mingling of two compositionally different magmas.

Chakhmouradian and Mitchell (2000) observed that enrichment in LREE, Th and Nb in perovskites is correlated neither with a particular facies of the kimberlite nor with a specific mineral paragenesis. Therefore it seems unlikely that coexistence of type Ia and Ib is just a consequence of mixing of facies within the same kimberlite. Degassing processes have been invoked previously to explain the occurrence of different populations of perovskite within the same kimberlite (Sarkar et al., 2011). In our work, it could be argued that the petrography supports a hypothetical two-stage crystallisation process in a degassing magma, in which type Ia perovskite would have crystallised prior to degassing, whereas type Ib perovskite would be the post-degassing phase. However, the lack of TiO_2 rims on type Ia perovskite, expected from devolatilization processes, as well as the composition of the type Ib perovskite (i.e. enriched in HFSE and REE) argue against the explanation by Sarkar et al. (2011). Moreover, Fe–Nb oxybarometry shows that the magma from which type Ib perovskite crystallised was slightly more reducing than that which crystallised type Ia. This is not consistent with a degassing process, which would typically lead to more oxidised

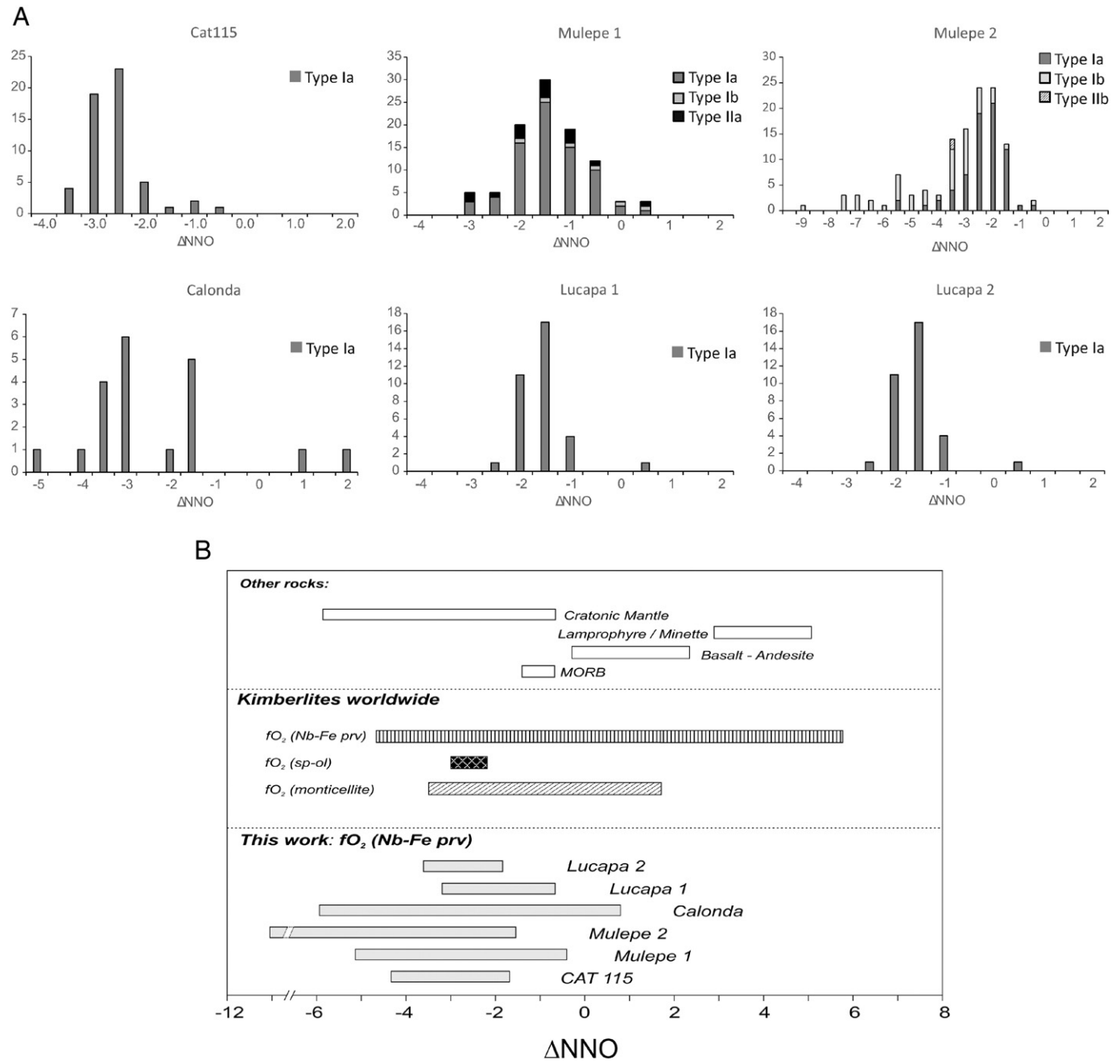

Fig. 7. (a) Frequency histograms of log fO_2 expressed relative to the NNO buffer (ΔNNO) calculated using the perovskite oxybarometer developed by Bellis and Canil (2007). The wider fO_2 range observed in the Mulepe 2 kimberlite results from the higher type 2 perovskite content in this kimberlite. (b) Comparison of the ΔNNO conditions recorded by the perovskite grains of the Angolan kimberlites with the data obtained from the literature and compiled by Canil and Bellis (2007) and Chalapathi Rao et al. (2013), including worldwide kimberlites, cratonic lithospheric mantle and mantle-derived magmas. With the exception of the Mulepe 2 pipe, in which some type Ib perovskite yield more reducing conditions, all kimberlites recorded oxygen fugacities within the range of the kimberlites from the literature. Additionally, the oxygen fugacities calculated by other oxybarometers are also included for comparison: spinel-olivine oxybarometer (Fedortchouk and Canil, 2004) and monticellite oxybarometer (Le Pioufle and Canil, 2012).

conditions in the remaining magma (Sarkar et al., 2011). Instead, it is more likely that the wide range of the oxygen fugacity displayed by groundmass perovskite of the Mulepe kimberlites resulted from the mingling of compositionally distinct magmas or multiple intrusion events (Eccles et al., 2004; Ogilvie-Harris et al., 2009).

The differences in composition between both types of perovskite also support a late incorporation of a more evolved melt previously enriched in these elements. Most grains of type Ia perovskite exhibit the "normal" zoning pattern described by Chakhmouradian and Mitchell (2001). The rimward sodium loss, coupled with a significant decrease in REE, Th and Ta, could be explained by progressive depletion in the kimberlitic melt during perovskite crystallisation (Chakhmouradian et al., 2013). Therefore, the high Na, REE and Nb contents reported in type Ib perovskite require the presence of a compositionally different magma from which type Ia perovskite crystallised.

Since perovskite crystallisation plays an important role in the fractionation of trace elements in kimberlite and carbonatite magmas during cooling (e.g. Beyer et al., 2013; Chakhmouradian et al., 2013), the trace-element composition of each population of perovskite could be used to infer the nature of the different melts in equilibrium at the moment of perovskite crystallisation. An inversion modelling of the perovskite trace element data was carried out, using the perovskite/kimberlite partition coefficients (D) proposed by Chakhmouradian et al. (2013). These coefficients are generally consistent with those

Table 6
Summary of U–Pb age of perovskites from the studied Angolan kimberlites. As shown in the table, the crystallisation age of type Ia and Ib perovskites of the Mulepe kimberlites was also calculated separately, but the values are still identical within uncertainty. *The ages reported for the Lucapa kimberlites are not reliable (see text for a better approximation).

	Age (Ma)	MSWD
CAT115	133 ± 10	2.2
Mulepe 1	116.2 ± 6.5	4.1
Mulepe 2	123 ± 3.6	5.9
Mulepe 2 (Ia)	*121 ± 10*	*4.2*
Mulepe 2 (Ib)	*121.6 ± 5.5*	*6.7*
Calonda	119.5 ± 4.3	6
Lucapa 1[a]	156.1 ± 9.7	1.4
Lucapa 2[a]	87 ± 10	3.9

[a] See discussion.

Table 7
Summary of Sr–Nd results of perovskites from the studied Angolan kimberlites.

Kimberlite	Mulepe 1	Mulepe 2	Lucapa 1	Cat115
Age (Ma)	116.2	123	135.7	133
n:	20	35	12	9
$^{87}Sr/^{86}Sr$	0.70361 ± 43	0.70308 ± 31	0.70323 ± 66	0.70405 ± 74
$^{87}Rb/^{86}Sr$	0.00043 ± 24	0.00070 ± 31	0.00033 ± 43	0.00099 ± 63
$^{87}Sr/^{86}Sri$	0.70361 ± 43	0.70308 ± 31	0.70323 ± 66	0.70405 ± 74
n:	14	34	9	14
$(^{143}Nd/^{144}Nd)$	0.51241 ± 27	0.51264 ± 8	0.51270 ± 23	0.51265 ± 21
$(^{147}Sm/^{144}Nd)$	0.0799 ± 18	0.08620 ± 49	0.08336 ± 71	0.07958 ± 47
$(^{143}Nd/^{144}Nd)_t$	0.51235 ± 28	0.51256 ± 8	0.51262 ± 23	0.51258 ± 21
$\varepsilon Nd_{(0)}$	−4.3 ± 5.4	0.1 ± 1.6	1.1 ± 4.5	0.2 ± 4.1
$\varepsilon Nd_{(t)}$	−2.6 ± 5.4	1.9 ± 1.6	3.1 ± 4.5	2.2 ± 4.1

n: number of analyses.
$\varepsilon Nd_{(t)} = (((^{143}Nd/^{144}Nd)_s - (^{147}Sm/^{144}Nd)_s \times (e^{\lambda t}-1))/((^{143}Nd/^{144}Nd)_{CHUR} - (^{147}Sm/^{144}Nd)_{CHUR} \times (e^{\lambda t}-1)) - 1) \times 10000$.
where s = sample; $(^{143}Nd/^{144}Nd)_{CHUR} = 0.512638$; and $(^{147}Sm/^{144}Nd)_{CHUR} = 0.1967$; $\lambda = 0.00654$/Ga for ^{147}Sm; t = age (in Ga) calculated for each kimberlite in this study.
$Sr_i = {}^{87}Sr/^{86}Sr_s - (^{87}Rb/^{86}Sr_s \times e^{\lambda t}-1)$.
Where s = sample; $\lambda = 0.01420$/Ga; t = age (in Ga) calculated for each kimberlite in this study.

obtained experimentally by Beyer et al. (2013). The composition of the melt in equilibrium with each perovskite type is represented in Fig. 5. The patterns of the resulting melts are very similar to that defined by whole rock analyses of kimberlite (Chakhmouradian et al., 2013), characterised by a 10× to 100× enrichment in incompatible elements (LILE and HFSE) relative to the primitive mantle. In general, the calculated melts are slightly further enriched in these incompatible elements compared to the whole rock analyses. This enrichment is significantly more important for some elements such as U, Nb, Zr and Hf, whereas the Th contents are lower than those found by whole rock analysis. As expected from their trace-element composition, the composition of the calculated melt in equilibrium with type Ib perovskite is more enriched in HFSE than that from which type Ia crystallised. The most relevant divergence between the calculated melt and the whole rock analyses is observed in type IIb perovksite, although given its small grain size the high Rb and K values are probably an artefact resulting from the ablation of groundmass phologopite.

There is also some evidence of a third melt that reacted with the groundmass minerals already crystallised. The Nb-rich perovskite (IIb) found rimming some type Ia perovskite in the Mulepe kimberlites is compositionally identical to those found in Lac de Gras (Canada) and

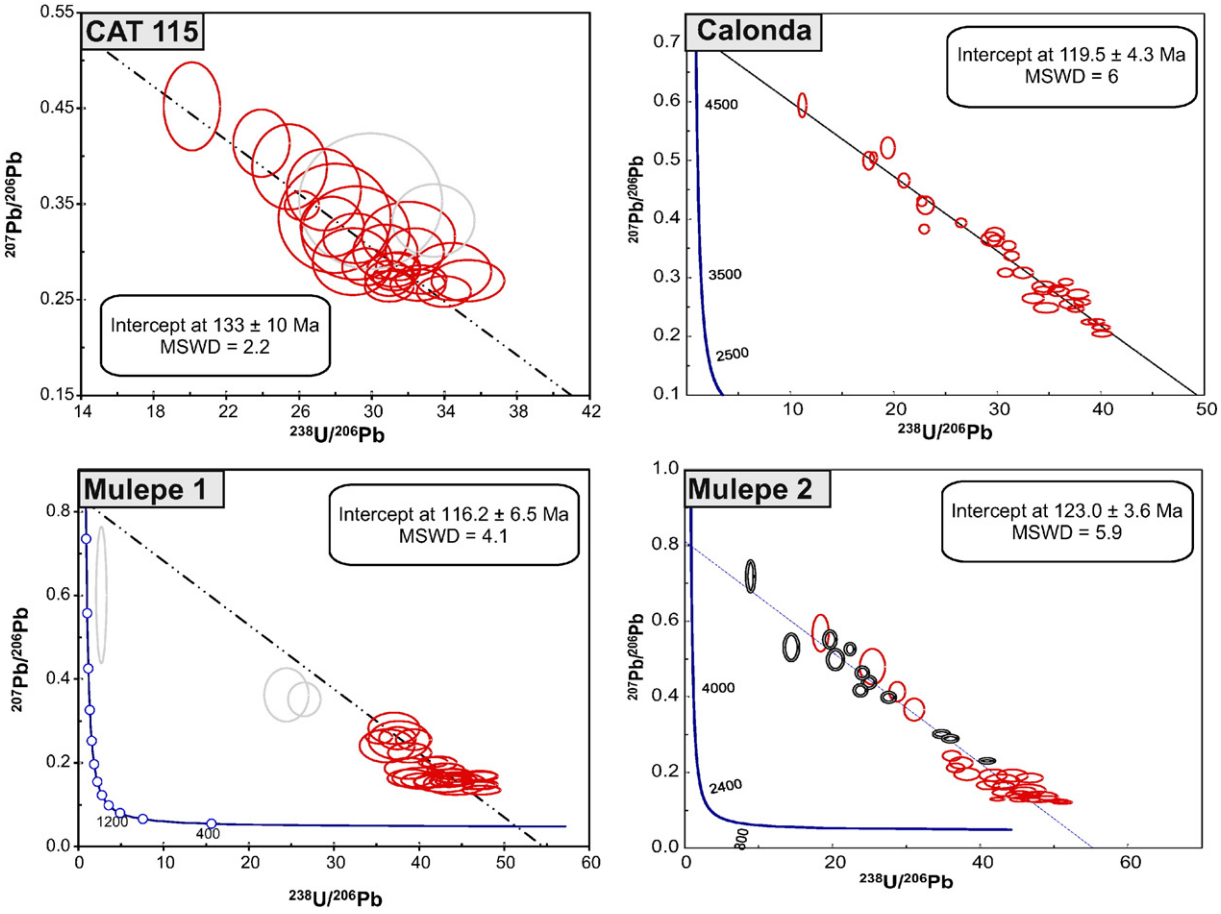

Fig. 8. Cat115, Calonda and Mulepe perovskite U–Pb data in inverse-Concordia (Tera–Wasserburg) plots. The lower intercept gives the age recorded by the perovskite grains of each pipe. Errors are shown as ellipses at 1σ. In the Mulepe 2 kimberlite, analysis corresponding to subtype Ib perovskite are represented by two concentric circles.

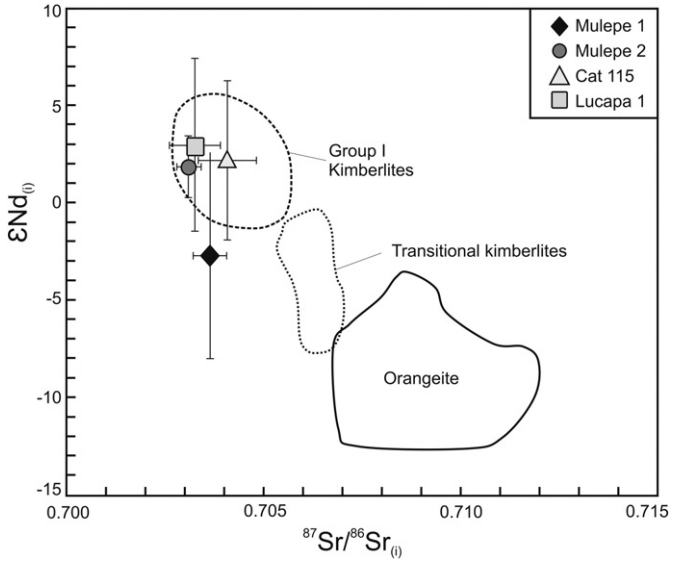

Fig. 9. εNd_i vs. $^{87}Sr/^{86}Sr_i$ average composition of groundmass perovskite from the Mulepe 1 and 2, Cat115 and Lucapa 1 kimberlites. Kimberlite, orangeite and transitional kimberlite fields from Donnelly et al. (2012) and references therein.

in Kuruman (South Africa) kimberlites (Donnelly et al., 2012; Chakhmouradian et al., 2013). These rims have been previously interpreted as due to an interaction with an evolved kimberlite melt, without contribution of a hydrous fluid. The early loss of fluid from the kimberlite magma could result in an increase of fluid-incompatible elements in the melt, which would explain the secondary formation of Nb-rich rims on the original groundmass perovskite (Chakhmouradian et al., 2013). Interestingly, the Nb-rich overgrowth in the Mulepe kimberlites is compositionally different to the average values for the type Ib perovskites found in the same pipes. These differences further support the hypothesis that the euhedral perovskites correspond to a completely different and independent magma, indicating that crystallisation of perovskite in Mulepe kimberlites was a multi-stage process. Additionally, the oscillatory zoning typical of the Mulepe kimberlites can be overprinted by more evolved compositions related to late processes. This supports a magmatic origin of the oscillatory zoning, related to the rapid crystallisation of the perovskite grain, regardless of further long-term interaction with a later more evolved kimberlitic magma. Our observations are consistent with several examples of mixing, mingling or scavenging in kimberlites, carbonatites and alkaline rocks (e.g. Ivanikov et al., 1998; Chakhmouradian and Mitchell, 2001; Zurevinski and Mitchell, 2004; Ogilvie-Harris et al., 2009; Tappe et al., 2009).

In any case, the ages calculated by U–Pb methods for both type Ia and Ib perovskite are identical within error and all the analyses fit the same regression line in the inverse-Concordia diagram, regardless of their texture (Fig. 8). Therefore, the lapse of time between the crystallisation of these two perovskite types should be less than 3My.

10.2. Age and tectonic implications

Structural control of kimberlite emplacement has been a matter of study for many years. There is a broad consensus that kimberlites are linked either to extensional episodes or reactivation of previous fault systems well after the main tectonic activity. Three different mechanisms are known to provide favourable conditions for kimberlite emplacement, always related to complex fault networks: i) supercontinent formation, ii) continental rifting and iii) late strain accommodation (Dawson, 1970; White et al., 1995; Jelsma et al., 2009; Tappe et al., 2014).

The ages reported for kimberlites in Angola, both in this study and in previously published work (Table 1), are not temporally linked to supercontinent assembly, but rather point to incipient rifting and strain accommodation. Continental break-up entails creation of a network of rift and fault zones as a consequence of extensional strain propagation into the supercontinent. During this stage pre-existing lithospheric discontinuities can also be reactivated and favour kimberlite emplacement. This seems to be the case for the studied kimberlites, which yield Early Cretaceous ages (115–130 Ma), coinciding with the break-up of Gondwana and the opening of the South Atlantic Ocean. The main eruptive age peak (120 Ma) correlates with the onset of spreading. This is also in very good agreement with other kimberlite magmatism in Africa, which is also related to NE–SW fault systems (Jelsma et al., 2004). Therefore as De Boorder (1982) suggested, deep-seated faults in Central Angola apparently played a major role in the emplacement of kimberlite and alkaline rocks. These structures delimit relatively narrow (50–90 km width) hidden corridors, or aulacogens, which are both chemically and physically different from the surrounding material. Jelsma et al. (2004) defined them as cryptic continental corridors and found that they are collinear with fracture zones along the Atlantic and Indian continental margins of Southern Africa; and are major features of the African lithospheric architecture (Begg et al., 2009).

The calculated U–Pb ages for the Angolan kimberlites are older than most of the Group I kimberlites in South Africa (Jelsma et al., 2004; Griffin et al., 2014), which would be consistent with a stress propagation and melt migration along deep fracture zones, related with the opening of the South Atlantic Ocean.

11. Conclusions

1. Perovskite is usually homogeneous in terms of major-element composition, but notable differences in trace-element patterns were observed among the Angolan kimberlites. This suggests that either the kimberlite source was heterogeneous at local scale and the magma composition changed through time, or that magma fractionation was significantly different between the kimberlites within the same area.
2. The Mulepe perovskites show a complex petrogenetic history. At least three different compositional and textural types of perovskite were identified within the same kimberlite, which has been explained by mingling of magmas differing in composition or in degree of evolution.
3. The kimberlite magmatism in the Lundas province (115–130 Ma) had the main eruptive peak around 120 Ma, coinciding with the Gondwana breakup. Kimberlite emplacement is explained by reactivation of NE–SW deep-seated faults, or cryptic continental corridors, which represent the continuation of the oceanic fracture zones.
4. The Sr_i and εNd_i values reported in the perovskites are in good agreement with the published data for on- and off-Craton South African Group I kimberlites.

Supplementary data to this article can be found online at http://dx.doi.org/10.1016/j.chemgeo.2015.12.014.

Acknowledgements

This research was supported by the projects CGL2006-12973 and CGL2009-13758 of the Ministerio de Ciencia e Innovación of Spain; the SGR 589, SGR 444 and 2014 SGR 1661 projects of the AGAUR-Generalitat de Catalunya; as well as funds from the ARC Centre of Excellence for Core to Crust Fluid Systems (CE110001017) of Excellence for Core to Crust Fluid Systems. Logistic assistance for the field trips was provided by the mining company CATOCA SL. The Ph.D. studies of M. Castillo-Oliver in Barcelona were supported by an FPU grant given by Ministerio de Ciencia e Innovación of Spain. The research activities were also funded by the Fundació Pedro Pons (UB), a research bursary

given by the Faculty of Geology from the Universitat de Barcelona and a Cotutelle International Macquarie University Research Excellence Scholarship (iMQRES–No. 2014210). The authors would also like to acknowledge Dr. Xavier Llovet and Dr. Eva Prats for their assistance with EMP and SEM analysis at the Serveis Científico-Tècnics (UB) and Dr. William Powell, Dr. Yoann Gréau, Dr. Rosanna Murphy and MSc. Sarah Gain for their help with the LA-ICP-MS analysis at the GEMOC (MQUni). This study used instrumentation funded by ARC LIEF and DEST Systemic Infrastructure Grants, Macquarie University, NCRIS AuScope and Industry. This is contribution 696 from the ARC Centre of Excellence for Core to Crust Fluid Systems (http://www.ccfs.mq.edu.au) and 1053 in the ARC National Key Centre for Geochemical Evolution and Metallogeny of Continents (http://www.gemoc.mq.edu.au). The authors would like to acknowledge the comments from the editor of Chemical Geology, Catherine Chauvel, as well as those from Sebastian Tappe and an anonymous reviewer, since they greatly improved the manuscript.

References

Batumike, J.M., Griffin, W.L., Belousova, E.A., Pearson, N.J., O'Reilly, S.Y., Shee, S.R., 2008. LAM-ICPMS U–Pb dating of kimberlitic perovskite: Eocene–Oligocene kimberlites from the Kundelungu Plateau, D.R. Congo. Earth Planet. Sci. Lett. 267, 609–619. http://dx.doi.org/10.1016/j.epsl.2007.12.013.

Becker, M., Le Roex, A.P., 2006. Geochemistry of South African on- and off-craton, group I and group II kimberlites: petrogenesis and source region evolution. J. Petrol. 47, 673–703. http://dx.doi.org/10.1093/petrology/egi089.

Begg, G.C., Griffin, W.L., Natapov, L.M., O'Reilly, S.Y., Grand, S.P., O'Neill, C.J., Hronsky, J.M.A., Djomani, Y.P., Swain, C.J., Deen, T., Bowden, P., 2009. The lithospheric architecture of Africa: seismic tomography, mantle petrology, and tectonic evolution. Geosphere 5, 23–50. http://dx.doi.org/10.1130/GES00179.1.

Bellis, A., Canil, D., 2007. Ferric iron in $CaTiO_3$ perovskite as an oxygen barometer for kimberlitic magmas I: experimental calibration. J. Petrol. 48, 219–230. http://dx.doi.org/10.1093/petrology/egl054.

Beyer, C., Berndt, J., Tappe, S., Klemme, S., 2013. Trace element partitioning between perovskite and kimberlite to carbonatite melt: new experimental constraints. Chem. Geol. 353, 132–139. http://dx.doi.org/10.1016/j.chemgeo.2012.03.025.

Black, L.P., Gulson, B.L., 1978. The age of the mud tank carbonatite, strangways range, Northern Territory. J. Aust. Geol. Geophys. 3, 227–232.

Canil, D., Bellis, A.J., 2007. Ferric iron in $CaTiO_3$ perovskite as an oxygen barometer for kimberlite magmas II: applications. J. Petrol. 48, 231–252. http://dx.doi.org/10.1093/petrology/egl067.

Carmichael, I.S.E., Nicholls, J., Smith, A.L., 1970. Silica activity in igneous rocks. Am. Mineral. 55, 246–263.

Chakhmouradian, A.R., Mitchell, R.H., 1998. Compositional variation of perovskite-group minerals from the Khibina complex, Kola peninsula, Russia. Can. Mineral. 36, 953–969.

Chakhmouradian, A.R., Mitchell, R.H., 2000. Occurrence, alteration patterns and compositional variation of perovskite in kimberlites. Can. Mineral. 38, 975–994. http://dx.doi.org/10.2113/gscanmin.38.4.975.

Chakhmouradian, A.R., Mitchell, R.H., 2001. Three compositional varieties of perovskite from kimberlites of the Lac de Gras field (Northwest Territories, Canada). Mineral. Mag. 65, 133–148.

Chakhmouradian, A.R., Reguir, E.P., Kamenetsky, V.S., Sharygin, V.V., Golovin, A.V., 2013. Trace-element partitioning in perovskite: implications for the geochemistry of kimberlites and other mantle-derived undersaturated rocks. Chem. Geol. 353, 112–131. http://dx.doi.org/10.1016/j.chemgeo.2013.01.007.

Chalapathi Rao, N.V., Wu, F.-Y., Mitchell, R.H., Li, Q.-L., Lehmann, B., 2013. Mesoproterozoic U–Pb ages, trace element and Sr–Nd isotopic composition of perovskite from kimberlites of the eastern Dharwar craton, southern India: distinct mantle sources and a widespread 1.1Ga tectonomagmatic event. Chem. Geol. 353, 48–64. http://dx.doi.org/10.1016/j.chemgeo.2012.04.023.

Corfu, F., Dahlgren, S., 2008. Perovskite U–Pb ages and the Pb isotopic composition of alkaline volcanism initiating the Permo-Carboniferous Oslo Rift. Earth Planet. Sci. Lett. 265, 256–269. http://dx.doi.org/10.1016/j.epsl.2007.10.019.

Cox, R.A., Wilton, D.H.C., 2006. U–Pb dating of perovskite by LA-ICP-MS: an example from the Oka carbonatite, Quebec, Canada. Chem. Geol. 235, 21–32. http://dx.doi.org/10.1016/j.chemgeo.2006.06.002.

Creaser, R.A., Gütter, H., Carlson, J., Crawford, B., 2004. Macrocrystal phlogopite Rb-Sr dates for the Ekati property kimberlites, Slave province, Canada: evidence for multiple intrusive episodes in the Paleocene and Eocene. Lithos 76, 399–414. http://dx.doi.org/10.1016/j.lithos.2004.03.039.

Davis, G.L., 1977. The ages and uranium contents of zircon from kimberlites and associated rocks. Extended Abstr., 2nd Int. Kimberlite Conf., Santa Fe, New Mexico.

Dawson, J.B., 1970. The structural setting of African kimberlite magmatism. In: Clifford, T.N., Gass, I.G. (Eds.), African Magmatism and Tectonics, pp. 321–335 (Edinburgh).

De Boorder, H., 1982. Deep-reaching fracture zones in the crystalline base-ment surrounding the west Congo system and their control of mineralization in Angola and Gabon. Geoexploration 20, 259–273.

Donnelly, C.L., Griffin, W.L., Yang, J.-H., O'Reilly, S.Y., Li, Q.-L., Pearson, N.J., Li, X.-H., 2012. In situ U–Pb dating and Sr–Nd isotopic analysis of perovskite: constraints on the age and petrogenesis of the Kuruman Kimberlite Province, Kaapvaal Craton, South Africa. J. Petrol. 53, 2497–2522. http://dx.doi.org/10.1093/petrology/egs057.

Eccles, D.R., Heaman, L.M., Luth, R.W., Creaser, R.A., 2004. Petrogenesis of the Late Cretaceous northern Alberta kimberlite province. Lithos 76, 435–459. http://dx.doi.org/10.1016/j.lithos.2004.03.046.

Egorov, K.N., Roman, E.F., Podvysotsky, V.T., Sablukov, S.M., Garanin, V.K., D'yakonov, D.B., 2007. New data on kimberlite magmatism in southwestern Angola. Russ. Geol. Geophys. 48, 323–336. http://dx.doi.org/10.1016/j.rgg.200.

Eley, R., Grütter, H., Louw, A., Tunguno, C., Twidale, J., 2008. Exploration geology of the Luxinga kimberlite cluster (Angola) with evidence supporting the presence of kimberlite lava. 9th Int. Kimberl. Conf. Ext. Abstr., pp. 1–3

Faure, S., 2010. World kimberlites CONSOREM database (version 3), consortium de recherche en exploration minérale CONSOREM. Université du Québec à Montréal ([WWW Document]. www.consorem.ca).

Fedortchouk, Y., Canil, D., 2004. Intensive variables in kimberlite magmas, Lac de Gras, Canada and implications for diamond survival. J. Petrol. 45, 1725–1745. http://dx.doi.org/10.1093/petrology/egh031.

Griffin, W.L., Powell, W.J., Pearson, N., O'Reilly, S.Y., 2008. GLITTER: data reduction software for laser ablation ICP-MS. In: Sylvester, P. (Ed.), Laser Ablation–ICP–MS in the Earth Sciences. Mineralogical Association of Canada Short Course Series, pp. 204–207.

Griffin, W.L., Batumike, J.M., Greau, Y., Pearson, N.J., Shee, S.R., O'Reilly, S.Y., 2014. Emplacement ages and sources of kimberlites and related rocks in southern Africa: U–Pb ages and Sr–Nd isotopes of groundmass perovskite. Contrib. Mineral. Petrol. 168 http://dx.doi.org/10.1007/s00410-014-1032-4.

Guiraud, R., Bosworth, W., Thierry, J., Delplanque, A., 2005. Phanerozoic geological evolution of Northern and Central Africa: an overview. J. Afr. Earth Sci. 43, 83–143.

Haggerty, S.E., Raber, E., Naeser, C.W., 1983. Fission track dating of kimberlitic zircons. Earth Planet. Sci. Lett. 63, 41–50. http://dx.doi.org/10.1016/0012-821X(83)90020-1.

Hawthorne, J.B., 1975. Model of a kimberlite pipe. Phys. Chem. Earth 9, 1–15. http://dx.doi.org/10.1016/0079-1946(75)90002-6.

Heaman, L.M., 1989. The nature of subcontinental mantle from Sr–Nd–Pb isotopic studies on kimberlitic perovskite. Earth Planet. Sci. Lett. 92, 323–334.

Ivanikov, V.V., Rukhlov, A.S., Bell, K., 1998. Magmatic evolution of the melilitite–carbonatite–nephelinite Dyke Series of the Turiy Peninsula (Kandalaksha Bay, White Sea, Russia). J. Petrol. 39, 2043–2059. http://dx.doi.org/10.1093/petroj/39.11-12.2043.

Jelsma, H.A., Wit, M.J.d., Thiart, C., Dirks, P.H.G., Viola, G., Basson, I.J., Anckar, E., 2004. Preferential distribution along transcontinental corridors of kimberlites and related rocks of southern Africa. S. Afr. J. Geol. 107, 301–324.

Jelsma, H., Barnett, W., Richards, S., Lister, G., 2009. Tectonic setting of kimberlites. Lithos 112, 155–165. http://dx.doi.org/10.1016/j.lithos.2009.06.030.

Kjarsgaard, B.A., Pearson, D.G., Tappe, S., Nowell, G.M., Dowall, D.P., 2009. Geochemistry of hypabyssal kimberlites from Lac de Gras, Canada: comparisons to a global database and applications to the parent magma problem. Lithos 112, 236–248. http://dx.doi.org/10.1016/j.lithos.2009.06.001.

Le Pioufle, A., Canil, D., 2012. Iron in monticellite as an oxygen barometer for kimberlite magmas. Contrib. Mineral. Petrol. 163, 1033–1046. http://dx.doi.org/10.1007/s00410-011-0714-4.

Le Roex, A.P., Bell, D.R., Davis, P., 2003. Petrogenesis of group I kimberlites from Kimberley, South Africa: evidence from bulk-rock geochemistry. J. Petrol. 44, 2261–2286. http://dx.doi.org/10.1093/petrology/egg077.

Ludwig, K.R., 2003. Isoplot/ex version 4.0: a geochemical toolkit for microsoft excel. Berkeley Geochronological Cent. Spec. Publ. 4, 1–70.

McDonough, W.F., Sun, S., 1995. The composition of the earth. Chem. Geol. 120, 223–253.

Mitchell, R.H., 1986. Kimberlites. Mineral., Geochem. Petrol.

Ogilvie-Harris, R.C., Field, M., Sparks, R.S.J., Walter, M.J., 2009. Perovskite from the Dutoitspan kimberlite, Kimberley, South Africa: implications for magmatic processes. Mineral. Mag. 73, 915–928. http://dx.doi.org/10.1180/minmag.2009.073.6.915.

Paton, C., Hergt, J.M., Phillips, D., Woodhead, J.D., Shee, S.R., 2007. New insights into the genesis of Indian kimberlites from the Dharwar Craton via in situ Sr isotope analysis of groundmass perovskite. Geology 35, 1011. http://dx.doi.org/10.1130/G24040A.1.

Pereira, E., Rodrigues, J., Reis, B., 2003. Synopsis of lunda geology, NE Angola: implications for diamond exploration. Comun. Inst. Geol. Min. 90, 189–212.

Perevalov, O.V., Voinovsky, A.S., Tselikovsky, A.F., Agueev, Y.L., Polskoi, F.R., Khódirev, V.L., Kondrátiev, A.I., 1981. Geology of Angola: Explanatory Notes of the Geological Map at a Scale of 1:1.000.000. Geological Survey of Angola, Luanda, Angola.

Pervov, V.A., Somov, S.V., Korshunov, A.V., Dulapchii, E.V., Félix, J.T., 2011. The Catoca kimberlite pipe, Republic of Angola: a paleovolcanological model. Geol. Ore Depos. 53, 295–308. http://dx.doi.org/10.1134/S1075701511040052.

Platt, R.G., 1994. Perovskite, loparite and Ba–Fe hollandite from the Schryburt Lake Carbonatite Complex, Northwestern Ontario, Canada. Mineral. Mag. 58, 49–57. http://dx.doi.org/10.1180/minmag.1994.058.390.05.

Pouchou, J.L., Pichoir, F., 1984. A new model for quantitative X-ray microanalysis. Part 1. Applications to the analysis of homogeneous samples. Rech. Aerosp. 11–38 (English Ed. 3).

Reguir, E.P., Camacho, A., Yang, P., Chakhmouradian, A.R., Kamenetsky, V.S., Halden, N.M., 2010. Trace-element study and uranium-lead dating of perovskite from the Afrikanda plutonic complex, Kola Peninsula (Russia) using LA-ICP-MS. Mineral. Petrol. 100, 95–103. http://dx.doi.org/10.1007/s00710-010-0131-9.

Reis, B., 1972. Preliminary note on the distribution and tectonic controls on kimberlites in Angola. 24th Int. Geollgical Congr. Montr. Section 4, pp. 276–281.

Robles-Cruz, S.E., Escayola, M., Jackson, S., Galí, S., Pervov, V., Watangua, M., Gonçalves, A., Melgarejo, J.C., 2012. U–Pb SHRIMP geochronology of zircon from the Catoca kimberlite, Angola: implications for diamond exploration. Chem. Geol. 310-311, 137–147. http://dx.doi.org/10.1016/j.chemgeo.2012.04.001.

Sarkar, C., Storey, C.D., Hawkesworth, C.J., Sparks, R.S.J., 2011. Degassing in kimberlite: oxygen isotope ratios in perovskites from explosive and hypabyssal kimberlites. Earth Planet. Sci. Lett. 312, 291–299. http://dx.doi.org/10.1016/j.epsl.2011.10.036.

Sarkar, Chiranjeeb, Storey, Craig D., Hawkesworth, Chris J., 2014. Using perovskite to determine the pre-shallow level contamination magma characteristics of kimberlite. Chem. Geol. 363, 76–90.

Smith, C.B., Allsopp, H.L., Gravie, O.G., Kramers, J.D., Jackson, P.F.S., Clement, C.R., 1989. Note on the U–Pb perovskite method for dating kimberlites: examples from the Wesselton and De Beers mines, South Africa, and Somerset Island, Canada. Chem. Geol. 79, 137–145.

Stacey, J.S., Kramers, J.D., 1975. Approximation of terrestrial lead isotope evolution by a two-stage model. 26, 207–221.

Storey, C.D., Smith, M.P., Jeffries, T.E., 2007. In situ LA-ICP-MS U–Pb dating of metavolcanics of Noorbotten, Sweden: records of extended geological histories in complex titanite grains. Chem. Geol. 163–181.

Sun, J., Liu, C.-Z., Tappe, S., Kostrovitsky, S.I., Wu, F.-Y., Yakovlev, D., Yang, Y.-H., Yang, J.-H., 2014. Repeated kimberlite magmatism beneath Yakutia and its relationship to Siberian flood volcanism: insights from in situ U–Pb and Sr–Nd perovskite isotope analysis. Earth Planet. Sci. Lett. 404, 283–295. http://dx.doi.org/10.1016/j.epsl.2014.07.039.

Sykes, L., 1978. Intraplate seismicity, reactivation of pre-existing zones of weakness, alkaline magmatism, and other tectonic postdating continental fragmentation. Rev. Geophys. Sp. Phys. 621–688.

Tappe, S., Simonetti, A., 2012. Combined U–Pb geochronology and Sr–Nd isotope analysis of the Ice River perovskite standard, with implications for kimberlite and alkaline rock petrogenesis. Chem. Geol. 304-305, 10–17. http://dx.doi.org/10.1016/j.chemgeo.2012.01.030.

Tappe, S., Foley, S.F., Jenner, G.a., Heaman, L.M., Kjarsgaard, B.a., Romer, R.L., Stracke, A., Joyce, N., Hoefs, J., 2006. Genesis of ultramafic lamprophyres and carbonatites at Aillik Bay, Labrador: a consequence of incipient lithospheric thinning beneath the North Atlantic Craton. J. Petrol. 47, 1261–1315. http://dx.doi.org/10.1093/petrology/egl008.

Tappe, S., Steenfelt, A., Heaman, L.M., Simonetti, A., 2009. The newly discovered Jurassic Tikiusaaq carbonatite-aillikite occurrence, west Greenland, and some remarks on carbonatite–kimberlite relationships. Lithos 112, 385–399. http://dx.doi.org/10.1016/j.lithos.2009.03.002.

Tappe, S., Pearson, D.G., Nowell, G., Nielsen, T., Milstead, P., Muehlenbachs, K., 2011. A fresh isotopic look at Greenland kimberlites: cratonic mantle lithosphere imprint on deep source signal. Earth Planet. Sci. Lett. 305, 235–248. http://dx.doi.org/10.1016/j.epsl.2011.03.005.

Tappe, S., Steenfelt, A., Nielsen, T., 2012. Asthenospheric source of Neoproterozoic and Mesozoic kimberlites from the North Atlantic Craton, West Greenland: new high-precision U–Pb and Sr–Nd isotope data on perovskite. Chem. Geol. 320-321, 113–127. http://dx.doi.org/10.1016/j.chemgeo.2012.05.026.

Tappe, S., Kjarsgaard, B.A., Kurszlaukis, S., Nowell, G.M., Phillips, D., 2014. Petrology and Nd–Hf isotope geochemistry of the neoproterozoic Amon Kimberlite Sills, Baffin Island (Canada): evidence for deep mantle magmatic activity linked to supercontinent cycles. J. Petrol. http://dx.doi.org/10.1093/petrology/egu048.

White, S.H., De Boorder, H., Smith, C.B., 1995. Structural controls of kimberlite and lamproite emplacement. J. Geochem. Explor. 53, 245–264.

Wiedenbeck, M., Alle, P., Corfu, F., Griffin, W.L., Meier, M., Oberli, F., Von Quart, A., Roddick, J.C., Spiegel, W., 1995. Three natural zircon standards for U–Th–Pb, Lu–Th, trace element and REE analyses. Geostand. Newslett. 19, 1–23.

Yang, Y.-H., Wu, F.-Y., Wilde, S.a., Liu, X.-M., Zhang, Y.-B., Xie, L.-W., Yang, J.-H., 2009. In situ perovskite Sr–Nd isotopic constraints on the petrogenesis of the Ordovician Mengyin kimberlites in the north China Craton. Chem. Geol. 264, 24–42. http://dx.doi.org/10.1016/j.chemgeo.2009.02.011.

Zurevinski, S.E., Mitchell, R.H., 2004. Extreme compositional variation of pyrochlore-group minerals at the Oka carbonatite complex, Quebec: evidence of magma mixing? Can. Mineral. 42, 1159–1168. http://dx.doi.org/10.2113/gscanmin.42.4.1159.